



# Diffusive-convection staircases in the polar oceans: the interplay between double diffusion and turbulence

Yuchen Ma<sup>1,†</sup> and W.R. Peltier<sup>1</sup>

<sup>1</sup>Department of Physics, University of Toronto, 60 St George Street, Toronto M5R2M8, ON Canada

(Received 18 May 2023; revised 23 January 2024; accepted 24 February 2024)

Numerical simulations have been conducted to examine the structure of diffusive-convection staircases in the presence of vortical-mode-induced turbulent forcing. By modulating the input power  $P$  and the background density ratio  $R_\rho$ , we have identified three distinct types of staircase structures in these simulations: namely staircases maintained in the system driven by double-diffusion, by turbulence or by a combination of both double-diffusion and turbulence. While we showed that staircases maintained in the double-diffusion-dominated system are accurately characterised by the existing model originally proposed by Linden & Shertcliffe (*J. Fluid Mech.*, vol. 87, no. 3, 1978, pp. 417–432), we introduced new physical models to describe the staircase structures maintained in the turbulence-dominated system and the system driven by both turbulence and double-diffusion. Our integrated model reveals that turbulence fundamentally governs the entire life cycle of the diffusive-convection staircases, encompassing their formation, maintenance and eventual disruption in the Arctic Ocean's thermohaline staircases. While our previous work of Ma & Peltier (*J. Fluid Mech.*, vol. 931, 2022*b*) demonstrated that turbulence could initiate the formation of Arctic staircases, these staircases are sustained by both turbulence and double-diffusion acting together after formation has occurred. Strong turbulence may disrupt staircase structures; however, the presence of weak turbulence could lead to unstable stratification within mixed layers of the staircases, as well as enhancing vertical heat and salt fluxes. Turbulence can even sustain a stable staircase structure factor when  $R_\rho$  is relatively large, following a similar mechanism to the density staircases observed in laboratory experiments. Consequently, previous parameterisations (e.g. Kelley, *J. Geophys. Res.: Oceans*, vol. 95, no. C3, 1990, pp. 3365–3371) on the

† Present address: Department of Earth, Atmospheric, and Planetary Sciences, Massachusetts Institute of Technology, 77 Massachusetts Ave., Cambridge, MA 02141, USA. Email address for correspondence: [yuchenma@mit.edu](mailto:yuchenma@mit.edu)

vertical heat flux across the diffusive-convection staircases may provide a significant underestimation of the heat transport by ignoring the influences of turbulence.

**Key words:** double diffusive convection, turbulent mixing, turbulence simulation

---

## 1. Introduction

Thermohaline staircases, characterised by alternating layers of homogeneous temperature and salinity with sharp interfaces separating adjacent mixed layers, are prevalent features in the Arctic Ocean. Because both temperature and salinity increase as depth in the stratification in the Arctic Ocean, this type of staircases were always referred to as ‘diffusive-convection staircases’, or ‘diffusive staircases’, to be distinguished from the ‘salt-fingering staircases’ in which both temperature and salinity decrease with depth (e.g. Radko 2013). First observed in the late 1960s (Neal, Neshyba & Denner 1969), our understanding of these Arctic staircases has grown significantly through the deployment of numerous ice-tethered profilers (e.g. Krishfield *et al.* 2008; Timmermans *et al.* 2008; Toole *et al.* 2011; Shibley *et al.* 2017) and an increasing number of microstructure measurements (e.g. Padman & Dillon 1989; Guthrie, Fer & Morison 2015; Fine *et al.* 2018, 2022; Boury *et al.* 2022). Recent studies, such as those by Shibley *et al.* (2017) and Van der Boog *et al.* (2021), have provided clear geographic maps illustrating the regions of existence these staircases, along with crucial information on interfacial thicknesses, layer depth and background density ratio.

Despite considerable advances in observing and measuring these staircase structures, at least three major theoretical questions remain to be addressed. (1) How do diffusive-convection staircases form? (2) How can we model the structure of these staircases? (3) How should we parameterise the vertical transport of heat and salt across these structures? These questions were raised and discussed shortly after the initial discovery of diffusive-convection staircases, as reviewed by Kelley *et al.* (2003). While progress has been made in answering each of these questions, further exploration is necessary. The third question is particularly crucial in the context of global warming, as the heat transport to the bottom of the sea ice in the Arctic Ocean is facilitated by these staircase structures (e.g. Rudels *et al.* 2004; Maksym 2019). Yet, to accurately address the third question, a comprehensive understanding of the answers to the first two questions is essential.

The formation mechanism of diffusive-convection staircases has traditionally been attributed to double-diffusion processes. Previously proposed mechanisms include the thermohaline-intrusion mechanism by Merryfield (2000) and Bebieva & Timmermans (2017), as well as the thermohaline-shear instability theory discussed in papers by Radko (2016), Brown & Radko (2019) and Radko (2019). However, these theories have limitations. The thermohaline-intrusion mechanism, for instance, provides only a rough description and lacks the necessary detail to accurately depict the formation of staircase structures. The thermohaline-shear instability theory, on the other hand, is limited by the specific form of shear and does not adequately describe general diffusive-convection systems.

In contrast to conventional understanding, our recent work (Ma & Peltier 2022*b*, hereafter MP21; Ma & Peltier 2022*c*, hereafter MP22) argues that stratified turbulence, rather than double-diffusion, may be the primary driver for the formation of diffusive-convection staircases. This theory demonstrates that the staircases will form spontaneously in a salinity-stratified ocean if the turbulent level is relatively low, which

explained the widespread availability of staircases in the Arctic Ocean where both these conditions are well met. Its central assumptions and conclusions have been further verified using a series of numerical simulations in MP22, establishing it as a highly plausible explanation for the formation of Arctic staircases.

Given our recent findings on the critical role of turbulence in the formation of staircase structures, a logical extension would be to explore its potential effect in sustaining these staircases and managing heat transport within them. Historically, many traditional studies, both in laboratory experiments and theoretical models, have overlooked turbulence. In the past, the characteristics of diffusive-convection staircases have been explored extensively through laboratory experiments, as evidenced by numerous studies such as Turner (1965), Shirtcliffe (1973), Crapper (1975), Marmorino & Caldwell (1976), Newell (1984), Taylor (1988) and, most recently, Guo, Cen & Zhou (2018). These investigations typically employed either heat–salt or salt–sugar systems to delve into the underlying dynamics and gauge vertical transport across the interfaces. Notably, mechanical forcing was absent in these set-ups. Based on these experimental results, empirical parameterisation schemes have been proposed to represent the heat and salt fluxes as a function of density ratio  $R_\rho = \Delta S / \Delta \Theta$  (here  $\Delta S$  and  $\Delta \Theta$  are differences between salinity and temperature between well-mixed layers, both defined in density units), for example Marmorino & Caldwell (1976), Kelley (1990) and the functional form used in the KPP parameterisation (Large, McWilliams & Doney 1994), which is the most commonly used parameterisation scheme in global climate models.

From a theoretical perspective, Linden & Shirtcliffe (1978) (hereafter LS) proposed a one-dimensional model to explain the maintenance of diffusive-convection staircases without invoking turbulence. In LS's model, steady diffusive-convection staircases can be sustained by the recurrent growth and disruption of unstable boundary layers at the edges of interfaces, if and only if the density ratio is smaller than the critical value of  $R_\rho^{cr} = \tau^{-1/2} \approx 10$ , where  $\tau = \kappa_s / \kappa_\theta \approx 0.01$  represents the ratio of molecular diffusivity for salinity to that for temperature under typical oceanographic conditions. The steadiness of these LS-like systems has been confirmed in several direct numerical simulations (DNS) study of (e.g. Flanagan, Lefler & Radko 2013; Sommer, Carpenter & Wüest 2014), in which staircase structures are in equilibrium under the condition of  $R_\rho < R_\rho^{cr}$ . The proposed boundary layer structures of LS has also been observed in the run-down DNSs of Carpenter, Sommer & Wüest (2012).

While these earlier investigations (including experiments, theories and simulations) demonstrated that steady staircase structure can indeed persist in the system without any mechanical forcing that drives turbulence, a growing interest has been focused on understanding the interactions between shear/turbulence and diffusive-convection staircases, given that real-world diffusive-convection staircases in the ocean are in the dynamic environment. In fact, observations have suggested that staircases in high shear environments might exhibit higher heat fluxes (e.g. Padman & Dillon 1987) and that stronger turbulence levels could lead to staircase disruption (e.g. Guthrie, Fer & Morison 2017). Numerical simulations have been employed to investigate the interaction between shear and double-diffusion staircases. For example, Brown & Radko (2021) and Brown & Radko (2022) have demonstrated that staircases are relatively resistant to shear-induced disruption and that heat and salt fluxes are enhanced in the presence of shear. Meanwhile, shear has also been identified as a potential cause of diffusive-convection layer formation in DNSs by Flanagan *et al.* (2014), Yang *et al.* (2022), Radko (2016) and Brown & Radko (2019). Regarding turbulence, its effects have been considered in the 1D model of Shibley & Timmermans (2019). Utilising this model and one-dimensional simulations, the authors

argued that in a weakly turbulent environment, a stable staircase structure might become unstable when weak turbulence is introduced, and the vertical heat fluxes would be even smaller than in the absence of turbulence.

In this paper, we present a systematic analysis of the interaction between turbulence and the diffusive-convection staircases using numerical simulations and theoretical models, seeking to understand the role of turbulence in maintaining the diffusive-convection staircase structures. Our numerical simulations build upon the methodologies established in our previous work MP22. In these simulations, vortical forcing, which is a representation of the influence exerted by large-scale geostrophic vortices (e.g. Waite & Bartello 2004) drives the triply periodic system that has a diffusive-convection type of stratification. A distinctive benefit of this forcing approach lies in its capability to meticulously modulate the turbulent intensity within the system by varying the strength of vortical-forcing implemented. Meanwhile, by adopting a triply periodic boundary condition, we eliminate unphysical responses from the simulation boundaries walls, providing a representation more in line with the Arctic pycnoclines. In MP22 we showed that staircase structures can form spontaneously from linear gradients of heat and salt in these models when subjected to intermediate strength of forcing, and we demonstrated that the formation mechanism is governed by the thermohaline-turbulence instability we initially proposed in MP21.

Based upon the same numerical model, we are able to further examine how the formed staircases react to varying turbulence intensities in our numerical systems. As we show in the following, staircases can be classified into different regimes based on different energy sources that drives the system: they can either be maintained in systems driven by double-diffusion, turbulence or driven by both. Staircases in these different regimes have different structures in mixed layers and interfaces, which further lead to distinct vertical transport of heat and salt. In contrast to Shibley & Timmermans's (2019) results, we show that heat and salt fluxes increase as the turbulent level increases in the system driven by both double-diffusion and turbulence.

In the remainder of this paper, we first provide a brief overview of our numerical simulation settings and categorise the simulation results into distinct regimes in § 2. Following that, in § 3, we develop models for diffusive-convection staircases in each of these regimes, based upon the findings of our numerical simulations. In § 4, we discuss the implications of our numerical simulations for actual staircases in the Arctic Ocean. Lastly, we present a summary and conclusion in § 5.

## 2. Different regimes of diffusive-convection staircases in numerical simulations

In this section, we focus on the settings and basic outcomes of numerical simulations performed in this paper. First, we introduce the settings and numerical method for the numerical simulations in § 2.1. Following this, we categorise the simulation results into five different regimes and present the typical evolution of the numerical system in each of these regimes in § 2.2. Lastly, in § 2.3, we display and compare the heat and salt fluxes across our simulations.

### 2.1. Numerical settings

The numerical model employed in this work closely resembles that in MP22. As in MP22, we assume constant-gradient background profile of  $-\Theta_{z0}$ ,  $-S_{z0}$  ( $\Theta_{z0} > 0$ ,  $S_{z0} > 0$ ) as the initial state, both of which increases with depth. Under the Boussinesq approximation, the scalar fields  $\Theta(x, y, z, t)$ ,  $S(x, y, z, t)$ , which are defined to be the

differences to these constant-gradient profiles, and the velocity field  $\mathbf{u}(x, y, z, t) = (u(x, y, z, t), v(x, y, z, t), w(x, y, z, t))$  are governed by the Navier–Stokes equations as follows:

$$\left. \begin{aligned} \frac{\partial \mathbf{u}}{\partial t} + \mathbf{u} \cdot \nabla \mathbf{u} &= -\nabla p - \left( \frac{R_\rho}{R_\rho - 1} S - \frac{1}{R_\rho - 1} \Theta \right) \mathbf{e}_z + \frac{1}{Re} \nabla^2 \mathbf{u} + \mathbf{F}, \\ \nabla \cdot \mathbf{u} &= 0, \\ \frac{\partial \Theta}{\partial t} + \mathbf{u} \cdot \nabla \Theta &= \frac{1}{RePr} \nabla^2 \Theta + w, \\ \frac{\partial S}{\partial t} + \mathbf{u} \cdot \nabla S &= \frac{1}{ReSc} \nabla^2 S + w. \end{aligned} \right\} \quad (2.1)$$

In the above equations,  $\mathbf{e}_z$  is the unit vector in the positive vertical direction. We have non-dimensionalised these equations using length scale  $L_0$ , temperature scale  $\Delta\Theta = \Theta_{z0}L_0$ , salinity scale  $\Delta S = S_{z0}L_0$ , density scale  $\Delta\rho = \Delta S - \Delta\Theta$  and background buoyancy frequency  $N = \sqrt{g\Delta\rho/(\rho_0L_0)}$  as the timescale. This results in a velocity scale  $U_0 = L_0N = \sqrt{g\Delta\rho L_0/\rho_0}$  that we employ more often to define our non-dimensional parameters. The critical non-dimensional parameters are the Reynolds number  $Re = U_0L_0/\nu$  (where  $\nu$  is the kinematic viscosity), inverse density ratio  $R_\rho = \Delta S/\Delta\Theta$ , Prandtl number  $Pr = \nu/\kappa_\theta$  and Schmitt number  $Sc = \nu/\kappa_s$  (where  $\kappa_\theta$  and  $\kappa_s$  are molecular diffusivities for heat and salt). In this paper, we fix the value of  $Re = 1000$ ,  $Pr = 7$  and  $Sc = 70$  to be consistent with the initial exploration in MP22. Here  $Re = 1000$  essentially determines the size of our chosen domain. In MP22 we have demonstrated using a controlled experiment that the domain size is tall enough to not influence the initial layer formation. The dimensional size of our domain size is discussed in detail in § 4. The critical non-dimensional value of  $R_\rho$  is varied and studied in our simulations. It is worth noting that  $Sc = 70$  is approximately an order smaller than its actual value in the ocean and we employed this compromised value due to the constraint of limited computational resources. The ‘+w’ terms on the right-hand side of the latter two equations come from the vertical advection of the background vertical gradients  $-\Theta_{0z}$  and  $-S_{0z}$  after non-dimensionalisation.

Governing equations (2.1) are integrated in a triply periodic cubic domain of length  $2\pi$  in each dimension. Vertical periodicity in  $\Theta$  and  $S$  infers that the background gradients  $-\Theta_{z0}$  and  $-S_{z0}$  remain constant, allowing only local scalar gradients to vary within the simulation. Such a model is generally referred to as ‘unbounded gradient model’ (e.g. Radko 2013) in the literature. This model offers an optimal framework for investigating oceanographic staircase phenomena, given its exclusion of specific solid boundaries, which are irrelevant in the oceanographic context, and its allowance for the potential equilibrium of a staircase state.

In MP22 and the current study, we introduce body forcing to our system as a means of energy injection, ensuring the system maintains an equilibrium state and emulating large-scale forcing. Specifically, we resort to a vortical-mode forcing, as referenced in Waite & Bartello (2004), Maffioli, Brethouwer & Lindborg (2016) and Howland, Taylor & Caulfield (2020), to simulate the eddy-driven forcing stemming from large-scale quasi-horizontal motion. It is pertinent to highlight that the stratified turbulence system can also sustain small-scale turbulent energy through the breaking of internal waves, leading to forcing with pronounced vertical motions. A comparative analysis between these two modes of forcing was recently conducted by Howland *et al.* (2020). They found that wave-forced simulations typically exhibit elevated potential energy and superior mixing efficiency relative to vortical-mode forcing simulations. However, the question regarding



which form of forcing is more physically apt for a small-scale numerical simulation remains unclear. In our work, we opt for the vortical forcing, primarily due to the pronounced stratification and subdued internal wave energy characteristic of the Arctic Ocean (e.g. Cole *et al.* 2018). It is worth noting that opting for a different mixing approach could potentially yield varied simulation outcomes. Specifically, we have adhered to the vortical-mode forcing schema as outlined in MP22, detailed as follows:

$$(F_x, F_y) = A \times \text{Real} \left( \sum_{2.5 \leq \sqrt{k^2 + l^2} \leq 3.5} (l, -k) e^{i(kx + ly + \phi_{k,l})} \right), \quad (2.2)$$

where  $k$  and  $l$  are the wave numbers in the  $x$  and  $y$  directions, respectively, and the phase  $\phi_{k,l}$  is chosen randomly at each time step. The amplitude of the forcing  $A$  above is adjusted to ensure the energy input rate  $p \equiv \langle \mathbf{u} \cdot \mathbf{F} \rangle$  remains constant at each time step (in this paper  $\langle \cdot \rangle$  represents the volume averages). We further define the relative energy input rate

$$P \equiv \frac{\langle \mathbf{u}^{dim} \cdot \mathbf{F}^{dim} \rangle}{\nu N^2}, \quad (2.3)$$

using dimensional physical quantities to quantify the relative strength of this energy input rate compared with the background stratification. Considering the choice of the non-dimensional parameter in this paper,  $P = Re \times p = 1000p$ . The scaled energy input rate  $P$  is of greater importance than the value of the input power  $p$  non-dimensionalised by our choice of scales, as  $P$  can be directly compared with the buoyancy Reynolds number

$$Re_b \equiv \frac{\epsilon^{dim}}{\nu N^2}, \quad (2.4)$$

of the system (here  $\epsilon^{dim}$  is the dimensional value of viscous dissipation), which controls the criterion of layering formation of the system as shown in MP21 and MP22.

In MP22, simulations with  $R_\rho = 2, 5, 8, \infty$  (which represents a single-component system stratified by salinity) and  $P = 10$  were conducted (noted as R2P10, R5P10, R8P10 and R $\infty$ P10 in what follows), which showed that equilibrium staircase structures formed spontaneously from the linear background temperature and salinity stratification. In this paper, we first performed two additional simulations with  $R_\rho = 3$  and 4 (R3P10 and R4P10) using the same initial conditions as described in detail in MP22 to explore the model dependence on  $R_\rho$  more accurately. Both of these new simulations demonstrated spontaneous staircase structure formation in our system, similar to the R5P10 simulation performed in MP22. We then used the equilibrium states of all these simulations (R2P10, R3P10, R4P10, R5P10, R8P10) as initial conditions and adjusted the input power  $P$  to different values to explore the staircase state's robustness to various energy levels.

All simulations were performed using open-source computational fluid dynamics software Nek5000 (Fischer *et al.* 2008). As in MP22, the simulations are initially performed at a resolution of  $350 \times 350 \times 350$  until the system reached a equilibrium state. A higher resolution of  $700 \times 700 \times 700$  was then employed to better characterise the equilibrium structure of the system. In this paper, we use the term 'intermediate-resolution simulations' to represent the long-time-period simulation under the  $350 \times 350 \times 350$  resolution, which is mostly relevant to § 2.2, focusing on the evolution process of staircases. Meanwhile, we use the term 'high-resolution simulations' to represent the shorter simulation under  $700 \times 700 \times 700$ , employed to better characterise the equilibrium structure of the staircase state, mainly discussed in §§ 2.3 and 3. It is important

Simulation	$R_\rho$	$P$	Initial condition	Run time	Final state	Staircases
R2P10 (MP22)	2	10	Linear gradient	3098	2 steps	Formed
R3P10	3	10	Linear gradient	12 526	1 step	Formed
R4P10	4	10	Linear gradient	10 918	1 step	Formed
R5P10 (MP22)	5	10	Linear gradient	8112	1 step	Formed
R8P10 (MP22)	8	10	Linear gradient	6298	1 step	Formed
R $\infty$ P10 (MP22)	$\infty$	10	Linear gradient	10 004	1 step	Formed
R2P0	2	0	R2P10 (2 steps)	4242	2 steps	Maintained
R2P1	2	1	R2P10 (2 steps)	1504	2 steps	Maintained
R2P5	2	5	R2P10 (2 steps)	1020	1 step	Merged
R2P50	2	50	R2P10 (2 steps)	1478	2 steps	Maintained
R2P100	2	100	R2P10 (2 steps)	510	0 step	Disrupted
R3P0	3	0	R3P10 (1 step)	1988	1 step	Maintained
R4P0	4	0	R4P10 (1 step)	2600	0 step	Disrupted
R5P0	5	0	R5P10 (1 steps)	6646	0 step	Disrupted
R5P1	5	1	R5P10 (1 step)	3288	0 step	Disrupted
R5P5	5	5	R5P10 (1 step)	2068	1 step	Maintained
R5P50	5	50	R5P10 (1 step)	898	1 step	Maintained
R5P100	5	100	R5P10 (1 step)	666	0 step	Disrupted
R8P0	8	0	R8P10 (1 step)	3016	0 step	Disrupted
R8P5	8	5	R8P10 (1 step)	1944	1 step	Maintained
R $\infty$ P0	$\infty$	0	R $\infty$ P10 (1 step)	4345	0 step	Disrupted
R $\infty$ P5	$\infty$	5	R $\infty$ P10 (1 step)	2572	1 step	Maintained
R $\infty$ P50	$\infty$	50	R $\infty$ P10 (1 step)	542	1 step	Maintained
R $\infty$ P100	$\infty$	100	R $\infty$ P10 (1 step)	428	0 step	Disrupted

Table 1. Governing parameters and critical information for the intermediate-resolution numerical simulations performed in this paper.

to note that while our high-resolution simulation adequately captures the Kolmogorov scale, the grid spacings employed are still 2–8 times larger than the Batchelor’s scale specific to salinity. Achieving an even finer resolution would necessitate substantially more computational resources than are currently accessible to us. A comprehensive discussion regarding the influence of resolution on the equilibrium state of our simulations can be found in the [Appendix](#). Although the current resolution might introduce small biases in the quantification of heat and salt transport, no significant differences were observed in the horizontally averaged vertical profiles of temperature and salinity at the equilibrium states in simulations of different resolutions.

In [table 1](#), we provide a concise summary of the parameters and the staircase state of all the simulations performed in the current paper, along with the four relevant simulations from MP22. As evident from the table, the fate of the staircases is strongly dependent on both the non-dimensional parameters  $R_\rho$  and  $P$ .

## 2.2. Maintenance and disruption of staircases in different regimes

Before discussing the simulation results summarised in [table 1](#) in detail, we would like to classify our numerical systems into three different regimes based on energetic considerations. This can be done by examining the evolution of the volume-averaged kinetic energy of the system  $K \equiv 1/2\langle |\mathbf{u}|^2 \rangle$ , which can be directly derived based on (2.1)

as

$$\begin{aligned} \frac{dK}{dt} &= p - F_b - \epsilon \\ &= p - (F_{b\theta} + F_{bs}) - \epsilon, \end{aligned} \tag{2.5}$$

where

$$\left. \begin{aligned} \epsilon &= \frac{2}{Re} \langle s_{ij} s_{ij} \rangle, \\ F_b &= F_{b\theta} + F_{bs}, \\ F_{b\theta} &= -\frac{1}{R_\rho - 1} \langle w' \Theta' \rangle, \\ F_{bs} &= \frac{R_\rho}{R_\rho - 1} \langle w' S' \rangle, \end{aligned} \right\} \tag{2.6}$$

are defined to be the viscous dissipation rate, total buoyancy flux (defined under the convention that buoyancy flux is positive if  $K$  loses energy) and buoyancy flux associated with temperature and salinity, respectively.  $s_{ij}$  is the strain rate tensor which is defined as  $1/2(\partial u_i/\partial x_j + \partial u_j/\partial x_i)$ . Note that in this paper, we use an overline to represent the horizontal average of a physical quantity and we use  $'$  to represent the deviations from it. In the quasi-steady state of the system, the kinetic energy  $K$  of the system remains roughly constant, which leads to a simple balance equation of

$$\epsilon \sim p + (-F_b). \tag{2.7}$$

This allows us to define three different regimes.

- (i) The double-diffusion driven regime, which is defined by  $-F_b \gg p > 0$ . This means the dissipation is roughly balanced by the negative buoyancy forcing which is released by the potential energy stored in the unstably stratified temperature component ( $\epsilon \sim -F_b$ ). This is the classical energetics of double-diffusive convection, and we say this system is ‘driven by double-diffusion’.
- (ii) The turbulence-driven regime. In this case, we have  $F_b > 0$  and  $\epsilon + F_b \sim p$ . This represents a system that is entirely driven by external forcing, and the turbulence cascades to be dissipated at the molecular scale and drives mixing in the process. We therefore say the system is ‘driven by turbulence’.
- (iii) The regime driven by both double-diffusion and turbulence, or hereafter the hybrid regime. This is characterised by a comparable value of  $-F_b > 0$  and  $p$ . In this third case, the system is driven by both external forcing  $p$  and a negative buoyancy forcing  $-F_b > 0$  together, both of which provide energy for the system to be dissipated.

With the above method of distinguishing among the energy sources, we are able to further categorise these simulations into five different scenarios based on their different energy sources and the simulation outcomes: the staircases can either be ‘maintained in the double-diffusion-dominated regime’, ‘maintained in the turbulence-dominated regime’, ‘maintained in the hybrid regime’, ‘disrupted by diffusion’ or ‘disrupted by turbulence’. In doing so, we aim to distinguish between the various mechanisms that either sustain or disrupt the staircases. In [figure 1](#), we show the evolution of buoyancy fluxes and vertical temperature and salinity profiles in five simulations, R2P0, R8P5, R2P5, R5P0 and R2P100, to illustrate those five scenarios, respectively. For each simulation, the driving force of the system can be confirmed by comparing  $p$  (black lines) with  $F_b$  (red line



## Diffusive-convection staircases in the polar oceans

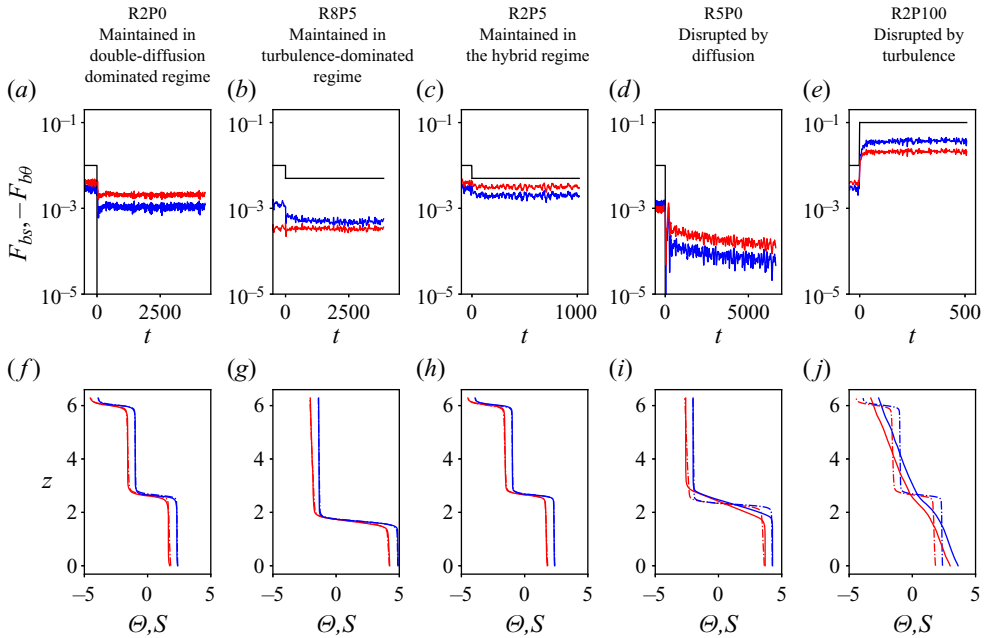


Figure 1. (a–e) Evolution of  $-F_{b\theta}$  (red) and  $F_{bs}$  (blue) in the intermediate-resolution simulations of R2P0, R8P5, R2P5, R5P0 and R2P100, respectively. The controlled input power of forcing  $p$  is also shown in each figure with a black line. (f–j) Comparisons of horizontally averaged profiles of temperature (red) and salinity (blue) at the beginning (dot-dashed lines) and the end (solid lines) of the intermediate-resolution simulations for R2P0, R8P5, R2P5, R5P0 and R2P100, respectively.

minus the blue line) in figure 1(a–e), and the evolution of the staircases can be seen in figure 1(f–j). As discussed previously and listed in table 1, the initial conditions for these five simulations were all set from the equilibrium stage of the previous staircase-forming simulations with  $P = 10$ , therefore  $p$  is adjust at  $t = 0$  in figure 1(a–e) to reflect these changes.

In cases where staircases are maintained, such as R2P0, R8P5 and R2P5, the system rapidly transitions to a new equilibrium state as the parameter  $P$  (or  $p$ ) is adjusted. Remarkably, the vertical structure of the staircases remains almost unchanged. The energy sources for R2P0, R8P5 and R2P5 are different, with R2P0 driven by double-diffusion, R8P5 driven by turbulence, and R2P5 driven by a combination of double-diffusion and turbulence. Although it is not immediately clear from figure 1, staircases with different energy sources actually have very different structures, and we examine these structures in detail in § 3 of this paper with our high-resolution simulations.

Now we turn to the cases in which staircases are disrupted when  $P$  is adjusted. In simulation R2P100 shown in figure 1(e,j), the forcing strength is sufficiently high to disrupt the staircase structure, leading the system to a turbulence-driven equilibrium state characterised by roughly linear temperature and salinity profiles. The staircase structure is entirely disrupted within approximately 50 time units (the relevant timescale in physical units is discussed in detail in § 4.1 of the current paper). In the case of simulation R5P0, the disruption process is driven by slow molecular diffusion at the interfaces, requiring a much longer time ( $O(100\,000)$  time units). Notably, by the end of the simulation, the disruption process is still ongoing, as demonstrated by the gradually diminishing buoyancy fluxes in figure 1(d).

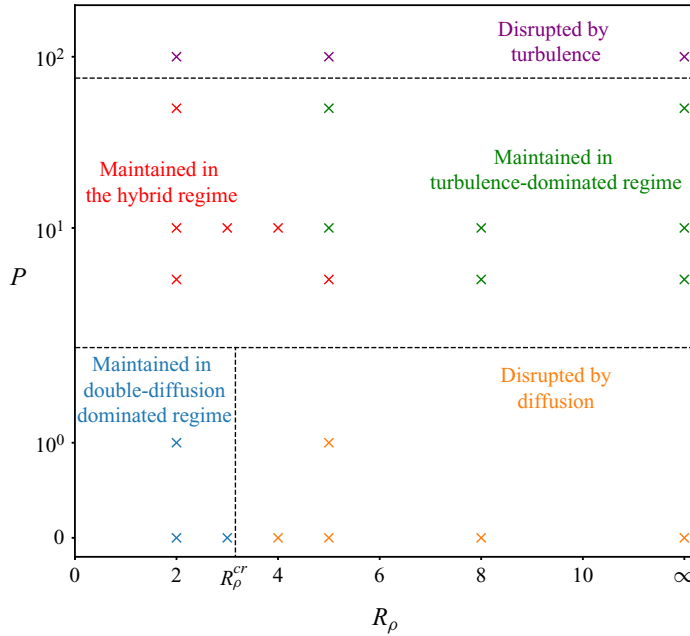


Figure 2. Classification of the simulation results for all the simulations described in table 1. Horizontal dashed lines represent the possible positions of the boundaries separating simulation results in different regimes. The vertical dashed line is plotted based on  $R_\rho = R_\rho^{cr} = \tau^{-1/2} \approx 3.16$ , which is the critical density ratio described in LS.

In figure 2, we plot all simulations listed in table 1 within the two-dimensional  $R_\rho$ – $P$  parameter space and categorise the results according to the five regimes previously discussed. When  $P$  is small, the system is predominantly driven by double-diffusion. In this scenario, the maintenance and disruption of staircases align with the classical critical density ratio criterion of LS: The staircase structure can be maintained only if  $R_\rho < R_\rho^{cr} = \tau^{-1/2} \approx 3.16$ . More investigations on the effectiveness of LS’s theory are performed in § 3.1.

However, as  $P$  increases to  $O(10)$ , the staircase structure can be maintained regardless of  $R_\rho$  values, because the intermediate strength of turbulence can lead to the stabilisation of the staircase structure. This effect has been discussed in MP22, and we further explore it in § 3. When  $P$  is on the order of  $O(10)$ , the system can be either driven by turbulence alone or driven by both double-diffusion and turbulence. It is important to note that the transition between the turbulence-dominated regime and the hybrid regime is distinguished by the sign of  $F_b$ . The boundary between these two regimes appears to depend on both  $R_\rho$  and  $P$ , so no simple boundary line can be drawn in figure 2.

In addition, while we labelled the R2P50 simulation as ‘maintained in the hybrid regime’, this specific simulation deviates from the evolution depicted in figure 1(c) and 1(h). In this case, the original two-layer staircases slowly merge into a single layer structure following the H merger mechanism described by Radko (2007) after we increase  $P$  from 10 to 50. A detailed analysis of the layer merging mechanism in our simulations and its dependence on external forcing falls outside the central focus of this paper, but may be examined in future studies.

Finally, when  $P$  increases to  $O(100)$ , the staircase structure will be disrupted by turbulence regardless of the values of  $R_\rho$ . This finding aligns with the conventional

understanding that staircase structures can often be disrupted by strong turbulence (e.g. Guthrie *et al.* 2017).

### 2.3. Heat and salt flux in the equilibrium stage of high-resolution simulations

While we have briefly discussed five different regimes for the evolution of staircases above, in this subsection, we focus on the vertical transport of heat and salt in these different regimes. To do this, we calculate the Nusselt numbers for salt  $Nu_s$  and heat  $Nu_\theta$ , and the flux ratio  $\gamma$  averaged in the equilibrium states of our high-resolution simulations as follows:

$$Nu_s = \frac{1}{ReSc} \langle \langle w'S' \rangle \rangle_t, \quad Nu_\theta = \frac{1}{RePr} \langle \langle w'\Theta' \rangle \rangle_t, \quad \gamma = \left\langle \frac{R_\rho \langle w'S' \rangle}{\langle w'\Theta' \rangle} \right\rangle_t, \quad (2.8a-c)$$

where we use  $\langle \rangle_t$  to represent time averages in this paper. Briefly put, Nusselt numbers describe the relative strength of vertical turbulent fluxes over the vertical diffusive fluxes, providing a convenient measurement of the strength of the vertical transport of heat and salt. The flux ratio  $\gamma$ , on the other hand, describes the relative strength of the salinity buoyancy flux over the temperature buoyancy flux. Therefore,  $\gamma > 1$  means  $F_b > 0$ , and  $\gamma < 1$  suggests  $F_b < 0$ . Consistent with classical definitions (e.g. Radko 2013), the occurrence of  $\gamma < 1$  in our system indicates that double-diffusion is playing a role so that the system lies either in the regime of ‘driven by double-diffusion’ or ‘driven by both turbulence and double-diffusion’.

In figure 3(a–c), we plot  $Nu_s$ ,  $Nu_\theta$ , and  $\gamma$  in the  $R_\rho$ – $P$  parameter space using different colour bars to represent their values. When directly comparing these quantities, it is important to note that these simulations lie in different regimes with varying staircase states, which might contribute to the differences in fluxes. It should also be mentioned that we are not evaluating the fluxes in regimes where staircases are disrupted by diffusion, given that the staircase disruption is so slow that no equilibrium state can be reached within a reasonable simulation time.

As shown in figures 3(a) and 3(b), both the Nusselt numbers  $Nu_s$  and  $Nu_\theta$  are positively related to  $P$ , and negatively related to  $R_\rho$ . Generally speaking,  $P$  has a stronger influence on the vertical transport of heat and salt than  $R_\rho$  does. In figure 3(c), we also show the value of  $\gamma$  for our simulations. As defined, the variation of  $\gamma$  is less than 1 in the double-diffusion maintained-staircase regime and jointly maintained regime and larger than 1 in the turbulence-driven regime. When turbulence is strong,  $\gamma$  can reach values close to  $R_\rho$ , suggesting a state in which turbulent diffusivities for heat and salt are almost identical, which is an assumption commonly made in strong turbulence.

In figures 3(d) and 3(e), we show the influence of  $P$  on  $Nu_\theta$  and  $Nu_s$  at fixed  $R_\rho = 2$  and  $R_\rho = 5$ , respectively. Turbulence influences the fluxes relatively weakly when the turbulent strength is weak and the system is still driven by double-diffusion, but this influence becomes much stronger at larger  $P$ . It is worth noting that the positive dependence of  $Nu_\theta$  on  $P$  in the low-turbulent regime of  $R_\rho = 2$  contradicts the previous model of Shibley *et al.* (2017), which predicted that turbulence would lead to a decrease of heat flux in the low-turbulence regime. This discrepancy may arise because the influence of turbulence in the mixed layers has not been properly considered in the previous model. A detailed analysis of the structure of thermohaline staircases driven by both turbulence and double-diffusion is presented in § 3.1.

In figure 3(f), we further explore the influence of  $R_\rho$  on  $Nu_\theta$  while keeping  $P = 10$  fixed. It is clear from the figure that as  $R_\rho$  increases,  $Nu_\theta$  will decrease (the higher value of  $Nu_\theta$  for  $R_\rho = 3$  than  $R_\rho = 2$  should be attributed to the consequence that the temperature

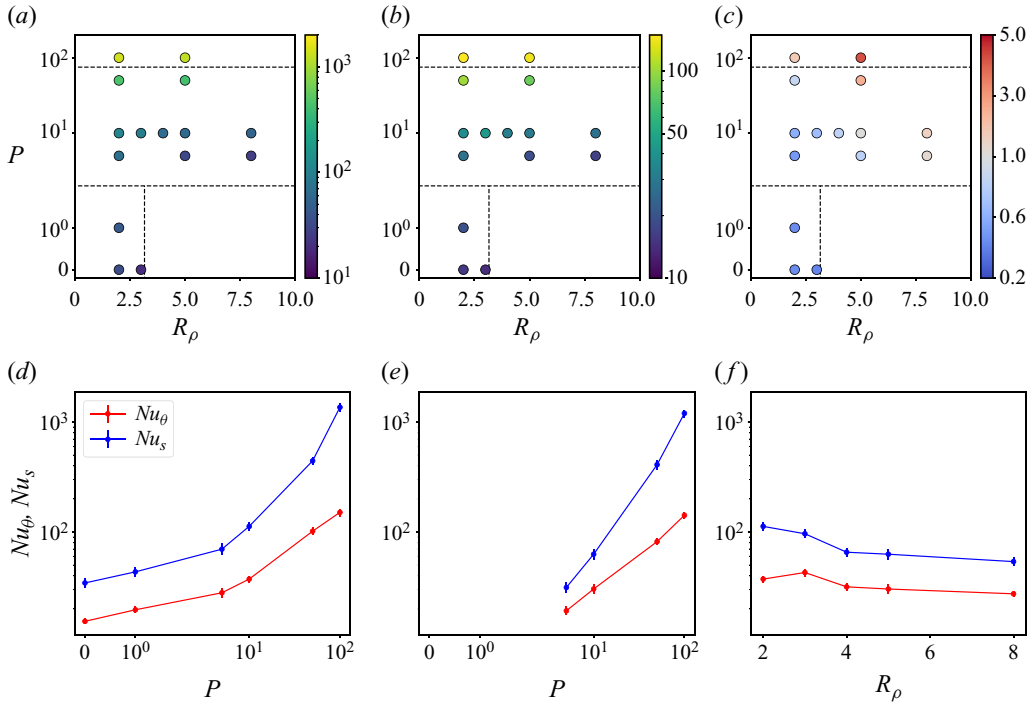


Figure 3. (a–c) Salinity Nusselt number  $Nu_s$  (a), temperature Nusselt number  $Nu_\theta$  (b) and flux ratio  $\gamma$  (c) averaged over equilibrium state of high-resolution simulations (simulations in the ‘disrupted by diffusion regime’ and simulations with  $R_\rho = \infty$  are not shown). (d) Variation of Nusselt numbers as a function of  $P$  for  $R_\rho = 2$ . (e) Variation of Nusselt numbers as a function of  $P$  for  $R_\rho = 5$ . (f) Variation of temperature Nusselt numbers as a function of  $R_\rho$  for  $P = 10$ . The errorbars in (d–f) are calculated based on the standard deviation of the Nusselt numbers in the equilibrium state of high-resolution simulations.

jump across the interfaces are smaller at  $R_\rho = 2$  because there are two steps). However, the influence of  $R_\rho$  on  $Nu_\theta$  is much weaker compared with  $P$ .

The comparisons presented above only reveal a general trend of how fluxes are impacted by the critical parameters  $R_\rho$  and  $P$ . An accurate functional form of the parameterisation cannot yet be properly calibrated based on these data, both because there are still some uncertainties related to the current resolution (discussed in the [Appendix](#)) and because we are currently assuming a compromised value of  $\tau$ , which leads to a much smaller  $R_\rho^{cr}$  than the oceanographic value.

Nonetheless, these comparisons still have crucial implications for the parameterisation of heat flux across diffusive-convection staircases. In previous studies, most parameterisation schemes are based on the study of purely double-diffusion-maintained staircases (e.g. Marmorino & Caldwell 1976; Kelley 1990; Flanagan *et al.* 2013). These parameterisations do not consider any large-scale forcing or energy sources, essentially setting  $P = 0$  and treating fluxes as functions of  $R_\rho$ , which, as discussed previously, plays only a secondary role in heat flux. By ignoring turbulence in this problem, these parameterisations may lead to a significant underestimation of vertical fluxes in the staircase state maintained in the hybrid regime. We revisit this issue in more detail in § 4.3 to systematically discuss the implications of our numerical simulations for actual oceanographic measurements in the Arctic staircases.

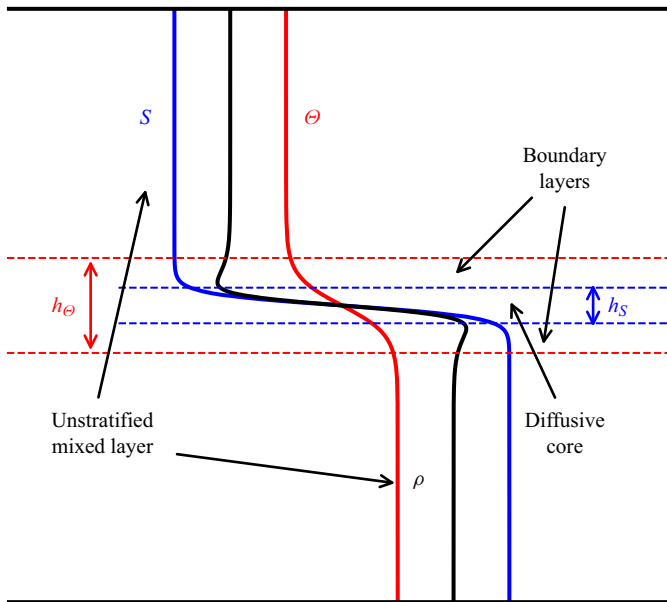


Figure 4. Schematic illustration of the diffusive interface model proposed by LS. Note that both potential temperature  $\Theta$  and  $S$  are in density units so that the equation of state takes the form of  $\rho = S - \Theta$ .

### 3. Structures of staircases in different regimes

In the previous section, we demonstrated that in our simulations, staircase structures can be maintained in the double-diffusion-dominated regime, maintained in the turbulence-dominated regime or maintained in the hybrid regime. In this section, we conduct a detailed investigation of the structures of these different types of staircases. Specifically, we will develop idealised models to describe their structures and then validate these models using data obtained from our high-resolution simulations.

#### 3.1. Staircases maintained in double-diffusion-dominated regime

The double-diffusion-dominated regime is characterised by low (or zero) external forcing. In this regime, the criterion for layer formation is highly consistent with the predictions of the theory of LS, as shown in figure 2. Therefore, it is instructive to briefly review the key physical descriptions of this model and compare the theoretical predictions with our numerical simulations.

LS proposed a classical model describing the structure of diffusive-convection staircases maintained under double-diffusion. As shown in figure 4, the diffusive-convection staircase structure proposed by LS consists of a diffusive core, two unstable boundary layers, and two unstratified well-mixed layers. In the diffusive core, LS assumed that heat and salt are transported only through molecular diffusion. Since the molecular diffusivity for temperature,  $\kappa_\theta$ , is much larger than that for salinity,  $\kappa_s$ , the interfacial thickness for temperature,  $h_\theta$ , is much larger than that for salinity,  $h_s$ . This leads to the formation of unstable boundary layers above and below the interfaces as demonstrated in figure 4. LS assumed that heat and salt transport from the interface into the mixed layers occurs through the continuous growth and breakdown of the boundary layer structure. Whenever the boundary layer becomes unstable enough to be disrupted down by convection, the heat and salt elements stored in the boundary layers are released into the upper (lower) mixed

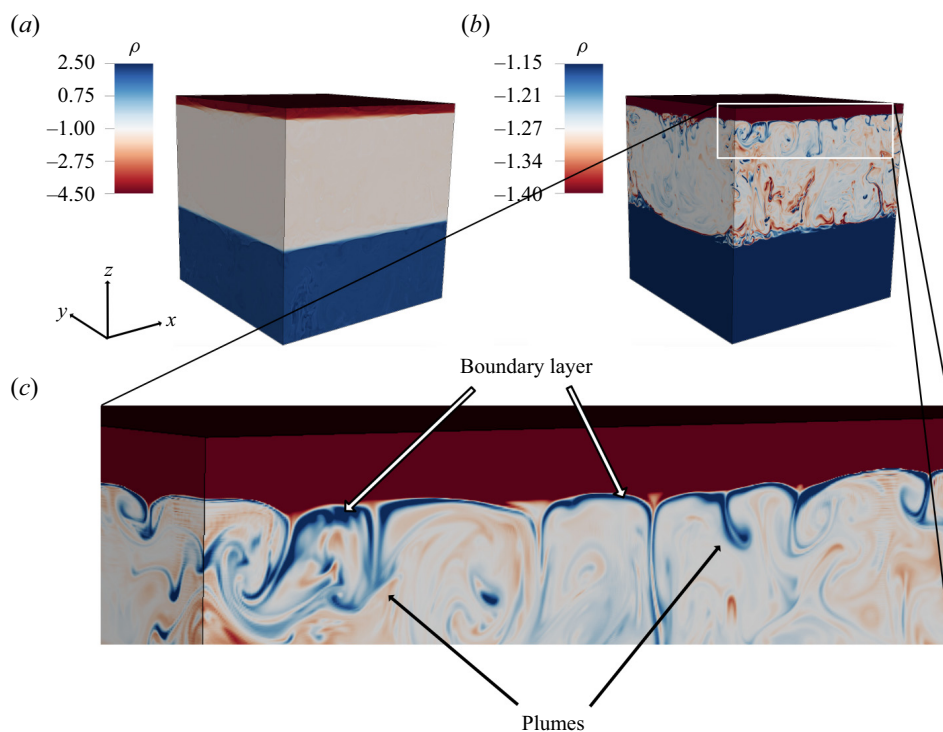


Figure 5. (a) Pseudo-colour plot of density fields for the equilibrium staircases in the high-resolution simulation of R2P0. (b) Same density field as (a), but with the colourbar adjusted to highlight the variations in the density field within the mixed layer. (c) Enlarged view of panel (b).

layer. By relating the diffusive fluxes to the fluxes generated by boundary layer instability, LS predicted that the structure is steady if and only if the density ratio  $R_\rho < R_\rho^{cr} = \tau^{-1/2}$ , where  $\tau = \kappa_s/\kappa_\theta$  is the diffusivity ratio, which has already been shown to be satisfied. The theory also demonstrated that the value of the local density ratio  $R_\rho^{loc}(z) = \bar{S}_z/\bar{\Theta}_z$  (here,  $S$  and  $\Theta$  are in density units) and flux ratio  $\gamma$  follow the relationship

$$\left. \begin{aligned} R_\rho^{loc} &= \tau^{-1/2} \\ \gamma &= \tau^{1/2} \end{aligned} \right\}, \quad (3.1)$$

at the interface.

The low-forcing simulations performed in this paper are largely consistent with the picture of LS’s theory described previously. This can be seen by first inspecting at the pseudo-colour plot of the density field at the equilibrium state of our high-resolution phase of simulation R2P0, shown in figure 5. While figure 5(a) shows two well-mixed layers with stable high-gradient interfaces present in our numerical system, the detailed structure in the mixed layers can be better visualised by adjusting the colourbar to focus on the mixed layer region, as in figures 5(b) and 5(c). In figure 5(c), we can clearly see a thin layer of heavier water (blue) just below the upper interface (the opposite is also true in the lower interface) as described by LS. Furthermore, these heavier elements sink into the mixed layer by the buoyancy forcing, generating thin plumes with buoyancy values different from the density of the mixed layers (rising plumes can also be seen in figure 5b). These plumes transport heat and salt between interfaces through mixed layers. The above



*Diffusive-convection staircases in the polar oceans*

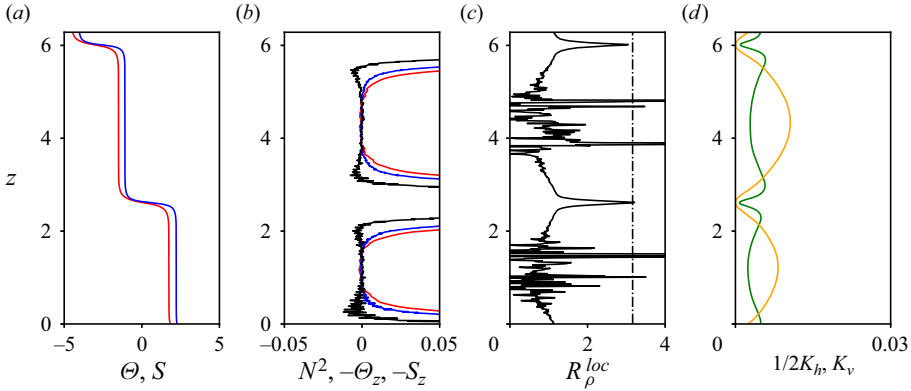


Figure 6. An example of the structure of staircase maintained in the double-diffusion-dominated regime in our numerical simulation. Depth dependence of temperature and salinity profile  $\Theta(z)$  (red),  $S(z)$  (blue) (a), buoyancy frequency  $N^2(z)$ , negative temperature and salinity gradients  $-\Theta_z$  (red) and  $-S_z$  (blue) (b), local density ratio  $R_\rho^{loc}(z)$  (c), half of the horizontal kinetic energy  $1/2K_h$  (green) and vertical kinetic energy  $K_v$  (yellow) (d), averaged over the equilibrium state of high-resolution simulation of R2P0. In (c), the dashed lines represent the values of  $R_\rho^{cr} = \sqrt{10} \approx 3.2$  predicted by LS's theory.

picture is generally consistent with LS's description, which claimed that the boundary layer would be constantly broken and inject heat and salt into the mixed layers.

The consistency with LS's theory can also be observed in the depth dependence of several physical quantities shown in figure 6. This figure displays the temperature and salinity profiles  $\Theta(z)$ ,  $S(z)$ , local buoyancy frequency  $N^2(z)$ , the local density ratio  $R_\rho^{loc}(z)$  and horizontal and vertical kinetic energies  $K_h(z)$  and  $K_v(z)$  for the high-resolution simulation of R2P0. Specifically, these physical quantities, together with the diapycnal diffusivities for heat and salt  $K_\Theta(z)$  and  $K_S(z)$  and the depth-dependent viscous dissipation rate  $\epsilon(z)$  that we evaluate in § 3.3, are evaluated based on time averages of the equilibrium stage of our high-resolution numerical simulation data as follows:

$$\Theta(z) = \overline{\langle \Theta(x, y, z, t) \rangle}_t, \tag{3.2a}$$

$$S(z) = \overline{\langle S(x, y, z, t) \rangle}_t, \tag{3.2b}$$

$$N^2(z) = - \left( \frac{R_\rho}{R_\rho - 1} \frac{\partial S(z)}{\partial z} - \frac{1}{R_\rho - 1} \frac{\partial \Theta(z)}{\partial z} \right), \tag{3.2c}$$

$$R_\rho^{loc}(z) = R_\rho \frac{\partial S(z)}{\partial z} \bigg/ \frac{\partial \Theta(z)}{\partial z}, \tag{3.2d}$$

$$K_h(z) = \frac{1}{2} \overline{\langle u^2(x, y, z, t) + v^2(x, y, z, t) \rangle}_t, \tag{3.2e}$$

$$K_v(z) = \frac{1}{2} \overline{\langle w^2(x, y, z, t) \rangle}_t \tag{3.2f}$$

$$K_\Theta(z) = - \overline{\langle w' \Theta'(z, t) \rangle}_t / \Theta_z(z) + \frac{1}{RePr}, \tag{3.2g}$$

$$K_S(z) = - \overline{\langle w' S'(z, t) \rangle}_t / S_z(z) + \frac{1}{ReSc}, \tag{3.2h}$$

$$\epsilon(z) = \overline{\langle 2s_{ij}s_{ij}(z, t) \rangle}_t, \tag{3.2i}$$

where we use overline to represent horizontal averages and we use subscript  $z$  to represent vertical derivatives.

In [figure 6\(a\)](#), it can be clearly seen that the mixed layers are essentially unstratified for both temperature and salinity profiles, which confirms the model shown in [figure 4](#). This fact is further verified in [figure 6\(b\)](#), in which the values of  $N^2(z)$  are approximately 0 in the mixed layers. The boundary layer structure is captured as small peaks of negative  $N^2(z)$  at the edges of mixed layers. In [figure 6\(c\)](#), we further plot the value of  $R_\rho^{loc}(z)$ , which matches quite well with LS's prediction (shown by the dot-dashed line) at the interfaces. [Figure 6\(d\)](#) shows the vertical structure of the distribution of  $K_h$  and  $K_v$ . The interface is almost motionless, especially for the vertical velocities, suggesting that the core of the interface is weakly influenced by the fluid motion in the mixed layer. In the mixed layers, on the other hand, the vertical motion is larger than the horizontal motion, consistent with the picture that vertical plumes driven by buoyancy forcing dominate the motion in the mixed layers.

While the above analyses provided further support on the effectiveness of LS's model in describing the staircase structure simulated in this paper, the flux ratio calculated from our numerical simulations do not agree well with LS's prediction. For example, the flux ratio  $\gamma$  is averaged to be approximately 0.45 at the equilibrium state in the high-resolution phase of the high-resolution simulation of R2P0, which is larger than the LS's predicted value of about 0.32. This fact could be due to the inaccurate estimations of scalar fluxes in our current simulations constrained by the resolutions. The evaluation of the influence of resolution on the equilibrium fluxes are discussed in detail in the [Appendix](#) of this paper.

### 3.2. Staircases maintained in the hybrid regime

In the last subsection, we demonstrated that the physics governing the staircase structures in the regime driven by double-diffusion can be well captured by the classic theory of LS. Now we examine staircases maintained in the system driven by both double-diffusion and turbulence to investigate how the introduction of turbulence influences the staircase structure. In fact, the staircase structure in this regime has been briefly analysed by investigating the simulation result of R2P10 in MP22, but we have not proposed any physical model of the staircase structure in MP22. In this paper, we discuss the key physical mechanism governing the staircase structure and perform further analyses on our simulations to test our proposed mechanism.

The basic staircase structure in this regime that we are proposing is shown in [figure 7](#). Similar to the staircase maintained only by double-diffusion ([figure 4](#)), there is an interface core through which heat and salt are transported mainly by molecular diffusion, although turbulence transport is also responsible for transporting some fluxes. The boundary layers can still be formed due to different values of diffusivities across the interface cores. However, under the influence of external forcing, finite values of temperature gradient and salinity gradient are present in the mixed layer region, the combined effect of which leads to the unstably stratified positive density gradient in the mixed layers, which is explained in what follows.

It should be noted that the scalar and density gradients in the mixed layers are exaggerated in [figure 7](#) to highlight their structural differences with [figure 4](#). The actual scalar gradients in our simulated staircase structure in this regime are still relatively small, as can be seen directly in the depth-dependent of scalar fields for simulation R2P5 shown in [figure 8\(a\)](#). In [figure 8\(b\)](#), we can still visualise the existence of boundary layer structure. In [figure 8\(c\)](#), we show the depth dependence of the local density ratio  $R_\rho^{loc}$ . In the mixed layers,  $R_\rho^{loc}$  is smaller than 1, which is another way of representing  $N^2 < 0$ . At the interface, LS's predicted value of  $\tau^{1/2}$  no longer provides a good estimate of  $R_\rho^{loc}$ , indicating that the

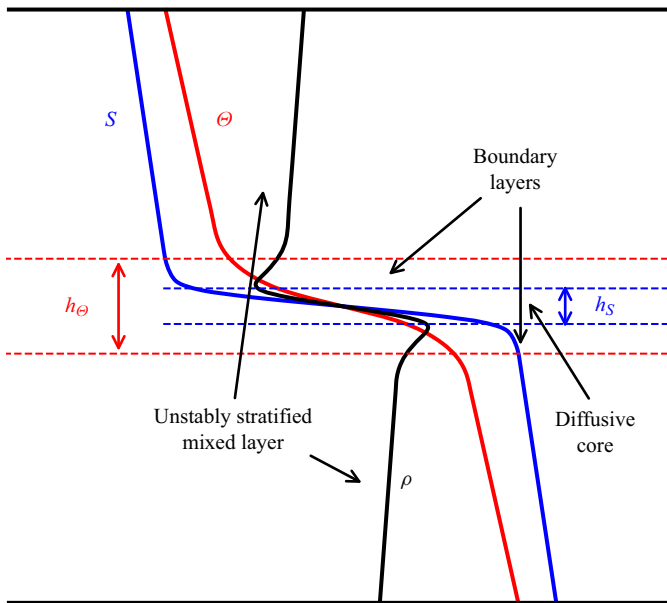


Figure 7. Schematic illustration of the staircase structure in the regime driven by both turbulence and double-diffusion.

turbulence introduced in the system start to influence the interface gradients by mixing scalar fields across it (the possible effect of turbulence penetration in leading to a larger  $R_{\rho}^{loc}$  can be found in discussion of MP22). In fact, the penetration of mixed layer motion at the interface can be seen in figure 8(d), where  $K_v$  and  $K_h$  are both larger at the interfaces compared with the double-diffusion-maintained interface shown in figure 6. More importantly, unlike figure 6(d), the mixed layer is dominated by horizontal motion instead of vertical motion, because we have employed vortical forcing on the system to stir the system into horizontal motion and the rising/sinking of plumes are no longer the dominant motion in the system.

One of the key questions for the staircase structure in this regime is to explain the existence of unstably stratified mixed layers. Insights on this question can be provided from the visualisation of the density field, shown in figure 9(b). Just as in the double-diffusion-maintained staircases, thin boundary layers that are lighter (heavier) than the mixed layers can also be seen directly above (below) the bottom (upper) interface. This is, again, due to the fact that heat diffuses much faster than salt, as shown schematically in figure 7. When the lighter (heavier) fluid elements rise (sink) from the boundary layer below (above) the mixed layer, the strong horizontal motion carries these fluid elements into the ambient environment at roughly the same height, helping spread these density anomalies. Meanwhile, the turbulent motion in the mixed layer region is also actively distorting the ‘abnormal’ densities in the boundary layers to the region that is just above or below the boundary layers. Under these influences, the upper mixed layers are turning ‘blue’ and the lower mixed layers are turning ‘red’ in figure 9(b), creating a negative  $N^2$  in the mixed layer region. Note that the mixing between boundary layer and mixed layer would not happen as strongly without the external forcing, as in figure 4. In that case, the mixed layer is dominated by the vertically oriented motion of plumes travelling across the mixed layer, without strongly interacting with the majority of mixed layer fluid elements.

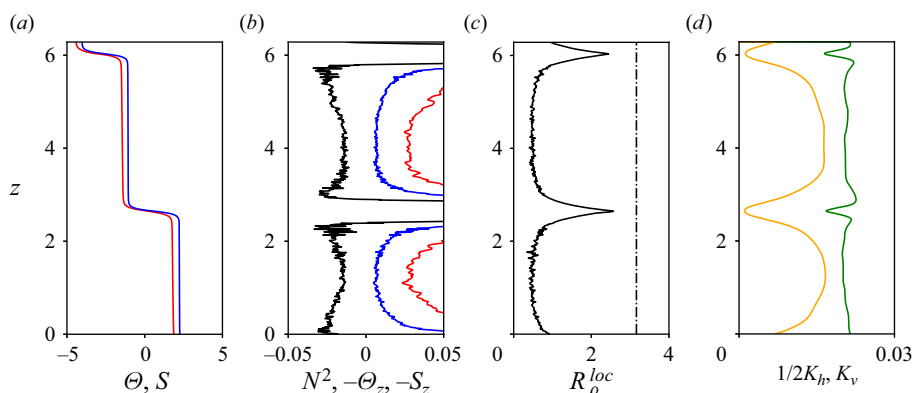


Figure 8. An example of the structure of staircase maintained in the hybrid regime in our numerical simulation. Depth dependence of temperature and salinity profile  $\Theta(z)$  (red),  $S(z)$  (blue) (a), buoyancy frequency  $N^2(z)$ , negative temperature and salinity gradients  $-\Theta_z$  (red) and  $-S_z$  (blue) (b), local density ratio  $R_\rho^{loc}(z)$  (c), half of the horizontal kinetic energy  $1/2K_h$  (green) and vertical kinetic energy  $K_v$  (yellow) (d), averaged over the equilibrium state of high-resolution simulation of R2P5. In (c), the dashed lines represent the values of  $R_\rho^{cr} = \sqrt{10} \approx 3.2$  predicted by LS's theory.

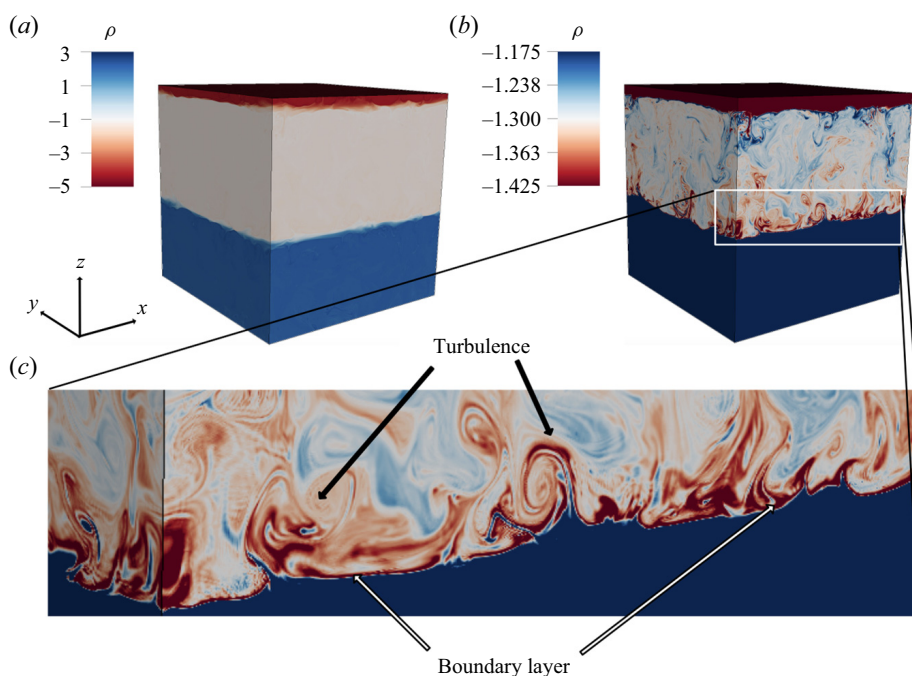


Figure 9. (a) Pseudo-colour plot of density fields for the equilibrium staircases in the high-resolution simulation of R2P5. (b) Same density field as (a), but with the colourbar adjusted to highlight the variations in the density field within the mixed layer. (c) Enlarged view of panel (b).

Given the unstable stratification of the mixed layer, Rayleigh–Bernard convection (e.g. Ahlers, Grossmann & Lohse 2009) also plays a role in facilitating mixing within this region. The convection-induced mixing tends to equalise diffusivities between heat and salt, thereby acting to neutralise the negative  $N^2$  present in the mixed layer.

However, in our simulations in which staircase are maintained in the hybrid system, the Rayleigh number for the mixed layer stratification stands at a modest value of the order of  $10^6$ , rendering the resultant convection insufficient to achieve total homogenisation of the mixed layers. Instead, this convection serves as an ancillary mechanism aiding in the transport of heat and salt within the mixed layer, complementing the mixing prompted by turbulence from horizontal motion and double-diffusion plumes. A precise quantification of the contributions from these mixing processes is intricate and strays from the central theme of this paper.

In summary, the incorporation of vortical mode forcing in our system generates turbulence within the mixed layers, significantly transforming the staircase structure observed in the double-diffusion case. On one hand, the turbulence permeates the interface and induces mixing across these interfaces. On the other hand, the turbulence blends the upwelling or downwelling boundary layer fluids with the nearby mixed layer fluid, resulting in a persistent unstably stratified density gradient within the mixed layer region. Consequently, the presence of this unstably stratified density gradient in the mixed layer should be regarded as a signature of turbulent mixing in the staircase structure.

### 3.3. *Staircases maintained in the turbulence-dominated system*

In the previous two subsections, we have discussed the structure of the staircases maintained in the double-diffusion-dominated regime and the hybrid regime. In this subsection we discuss the staircases maintained in the turbulence-dominated regime. In this regime, the energy is supplied by external forcing and the potential energy becomes a sink rather than source of the kinetic energy.

As in the previous two sections, we provide a brief sketch of the staircase structure to illustrate the key physical mechanisms that contribute to maintaining its stability. This sketch is shown in an exaggerated manner in [figure 10](#). The turbulence-maintained staircase structure is relatively simple: it consists of a weakly stratified mixed layer and a strongly stratified interface. The strongly stratified interface is still dominated by molecular diffusion, just like the previous two structures; however, the weakly stratified mixed layer sustains fluxes due to stratified turbulence. Since the mixed layer is weakly stratified, high values of diapycnal diffusivities are permitted to exist, which provide the fluxes needed to balance the diffusion-dominated fluxes across the high-gradient interfaces. The boundary layer structure, which played a dominant role in the previous two regimes, is absent in the turbulence-driven regime. This absence is due to the high density ratio in this regime, ensuring that the stably stratified salinity component consistently prevails over the unstably stratified temperature component, as demonstrated in [figure 10](#). In fact, the presence of the boundary layer structure is always associated with the release of potential energy, which will not occur in the turbulence-driven regime by definition.

The proposed structure is validated by the depth-dependent profiles observed in simulations R8P5 and R∞P5, as illustrated in [figure 11](#). In [figure 11\(a\)](#) corresponding to the R8P5 simulation, both  $\Theta$  and  $S$ , as well as  $\rho$ , consistently decrease with height. This monotonic decrease permits the use of a log-scale  $x$ -axis to more effectively capture the variations of stratification in [figure 11\(b\)](#). Notably, these turbulence-maintained staircases lack any boundary layer structures, consistent with the argument we made previously. A very similar staircase structure is evident in the R∞P5 simulation, as depicted in [figures 11\(d\)](#) and [11\(e\)](#). For the R∞P5 scenario, the system reverts to a single-component system where the stratification is only influenced by salinity. A comparison of the salinity stratification between R8P5 and R∞P5 reveals that incorporating a minor temperature component in R8P5 does not drastically alter the balanced salinity stratification observed

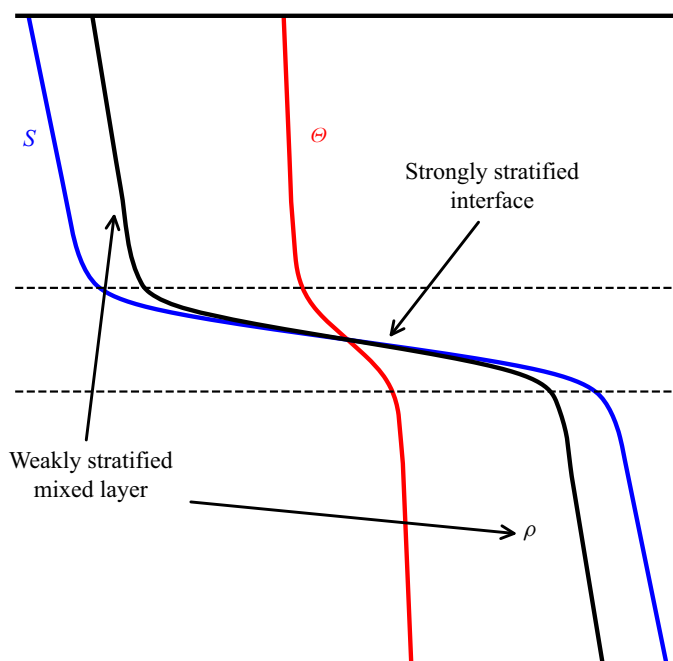


Figure 10. Schematic illustration of the staircase in the turbulence-driven regime. Note that both potential temperature  $\Theta$  and  $S$  are in density units so that the equation of state takes the form of  $\rho = S - \Theta$ .

in  $R\infty P5$ . However, it does act to weaken the density stratification within the mixed layer as the temperature component is unstably stratified.

The fact that staircases can be maintained in the single-component system  $R\infty P5$  demonstrates that the underlying mechanism that maintains the stable staircase structure in this regime is unrelated to double-diffusion and the maintenance mechanism operative in the single-component scenario is fundamental to the persistence of these staircases. The resemblance in staircase structure between  $R8P5$  and  $R\infty P5$  showed that the additional temperature component in the large- $R_\rho$  turbulent-driven staircases (e.g.  $R8P5$  and  $R8P10$ ) could be perceived as a deviation from the dominant balance established in the single-component system.

The persistence of the staircase structure in the turbulence-driven regime relies on the balance of fluxes between the mixed layer and interfaces. This was previously discussed in MP22, and we provide a brief overview here. As shown in figures 11(c) and 11(g), turbulent diapycnal diffusivities are markedly high within the mixed layers. Notably, the diffusivities for both heat and salt are nearly identical, which is consistent with the characteristics of high- $Re_b$  stratified turbulence in the weakly stratified environment (e.g. Shih *et al.* 2005). Meanwhile, the diapycnal diffusivities at the interfaces are close to the values of molecular diffusivities for heat and salt, respectively, as shown in the vertical dashed lines. Given that vertical heat and salt fluxes are the product of turbulent diffusivities and the corresponding vertical gradient, the pronounced diapycnal diffusivities present in the low-gradient mixed layers can produce fluxes that offset the diffusive fluxes transported through the high-gradient interfaces.

While balancing the fluxes is essential, it is not the only requirement for maintaining the staircases. The structure also needs to remain stable in the face of perturbations. In the rest of this subsection, we analyse the stability of turbulence-maintained staircases, providing



*Diffusive-convection staircases in the polar oceans*

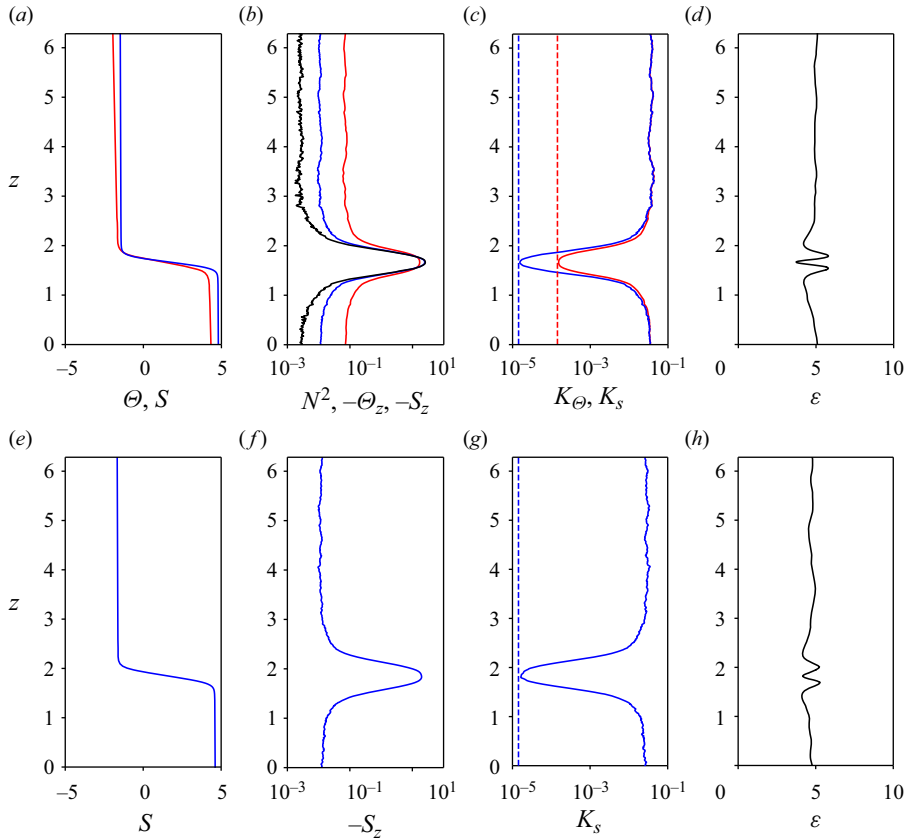


Figure 11. Examples of the structure of staircase maintained in the turbulence-dominated regime in our numerical simulation. Depth dependence of temperature and salinity profile  $\Theta(z)$  (red),  $S(z)$  (blue) (a,e), buoyancy frequency  $N^2(z)$ , negative temperature and salinity gradients  $-\Theta_z$  (red) and  $-S_z$  (blue) (b,f), turbulent diapycnal diffusivities  $K_\Theta$  and  $K_S$  (c,g) and viscous dissipation (e,h) for simulation R8P5 (a–d) and R $\infty$ P5 (e–h), respectively. All these quantities are non-dimensionalised versions of the corresponding physical quantities as defined previously in (3.2). The dashed lines in (c,g) represent the non-dimensional values for the molecular diffusivities for heat and salt in the current system.

(at least) a qualitative understanding of why the staircase structure is consistently disrupted under strong forcing, as depicted in figure 2.

To comprehend the stability of the turbulence-maintained staircases, we consider three simplifying assumptions.

- (i) The influence of temperature on density is disregarded (i.e.  $R_\rho = \infty$ ). As we discussed previously, the single-component system contains the essential dynamics in which staircases are maintained and large  $R_\rho$  simulations can be regarded as perturbations from this specific scenario.
- (ii) The dissipation rate  $\epsilon$  is assumed to be a constant  $\epsilon_0$ , which is determined by the external forcing  $p$  and remains the same value in mixed layers and at interfaces. This assumption is supported by our numerical simulations, as illustrated in figure 11(d,h).
- (iii) The diapycnal diffusivities in both the mixed layers and the interfaces are presumed to be governed by the parameterisation scheme proposed by Bouffard &

Boegman (2013). Specifically, Bouffard & Boegman (2013) introduced a parameterisation based on an extensive dataset from numerical simulations, which relies on the buoyancy Reynolds number  $Re_b$  and the Prandtl number  $Pr$ :

$$K_{\rho}^{BB}(Re_b, Pr) = \begin{cases} \kappa, & \text{if } Re_b < 10^{2/3}Pr^{-1/2}, \\ \frac{0.1}{Pr^{1/4}}\nu Re_b^{3/2}, & \text{if } 10^{2/3}Pr^{-1/2} < Re_b < (3 \ln \sqrt{Pr})^2, \\ 0.2\nu Re_b, & \text{if } (3 \ln \sqrt{Pr})^2 < Re_b < 100, \\ 2\nu Re_b^{1/2}, & \text{if } Re_b > 100, \end{cases} \quad (3.3)$$

where  $\kappa$  is the molecular diffusivity for density in the single-component fluid. The parameterisation presented forms the foundation of the thermohaline turbulence instability theory proposed in MP21. In MP22, it was demonstrated that this parameterisation provides a reasonable representation of mixing in the vortical-mode-forcing system (refer to figure 5 in MP22). Crucially, the parameterisation scheme reveals the existence of four distinct mixing regimes, where diapycnal diffusivities depend on varying power laws of  $Re_b$ . In increasing order of  $Re_b$ , these regimes are termed as ‘molecular regime’, ‘buoyancy-controlled regime’, ‘transitional regime’ and ‘energetic regime’, signifying the governing physics that define the respective power laws. For simplification purposes, we employ Greek letters I, II, III and IV to denote these four regimes in ascending order of  $Re_b$ .

Considering these three assumptions, the density fluxes for both the interface and mixed layer can be directly calculated by incorporating a  $Pr$  value of 70 for salinity (the value chosen for our simulations in the current paper) into the given equation, which yields

$$F_{\rho}^{BB}(Re_b) = -K_{\rho}^{BB} \rho_z = \begin{cases} 0.014 \frac{\epsilon_0 \rho_0}{g} Re_b^{-1}, & \text{if } Re_b < 0.56, \\ 0.035 \frac{\epsilon_0 \rho_0}{g} Re_b^{1/2}, & \text{if } 0.56 < Re_b < 41, \\ 0.20 \frac{\epsilon_0 \rho_0}{g}, & \text{if } 41 < Re_b < 100, \\ 2.0 \frac{\epsilon_0 \rho_0}{g} Re_b^{-1/2}, & \text{if } Re_b > 100. \end{cases} \quad (3.4)$$

The functional dependence mentioned previously is plotted in figure 12(a,b), which distinctly exhibits four different regimes of flux variations based on the value of  $Re_b$ . For mixed layers, the stratification is weak, resulting in a high enough  $Re_b$  to reach region IV (marked by letter ‘L’ in figure 12a,b). However, depending on the actual value of the density gradient at the interface,  $Re_b$  at the interfaces may be in either region I (figure 12a) or region II (figure 12b). In both cases, there is a possibility for  $F_{\rho}$  at the interface to balance that in the mixed layers.

Consider the perturbation (solid line) that we assumed to the original density stratification (dashed line) in figure 12(c,d). Such a perturbation results in an increase of the density gradient  $|\rho_z^L|$  in the mixed layer, as well as a decrease of  $|\rho_z^I|$  at the interface. In the mixed layers, the increase of  $|\rho_z^L|$  leads to a smaller  $Re_b$  and consequently an increase in  $F_{\rho}^L$ . In the case illustrated by figure 12(a), where the interface remains in region I, the decrease of  $|\rho_z^I|$  causes a reduction of  $F_{\rho}^I$ . The differences between  $F_{\rho}^L$  and  $F_{\rho}^I$  contribute to the accumulation of density below the interface and the depletion of density

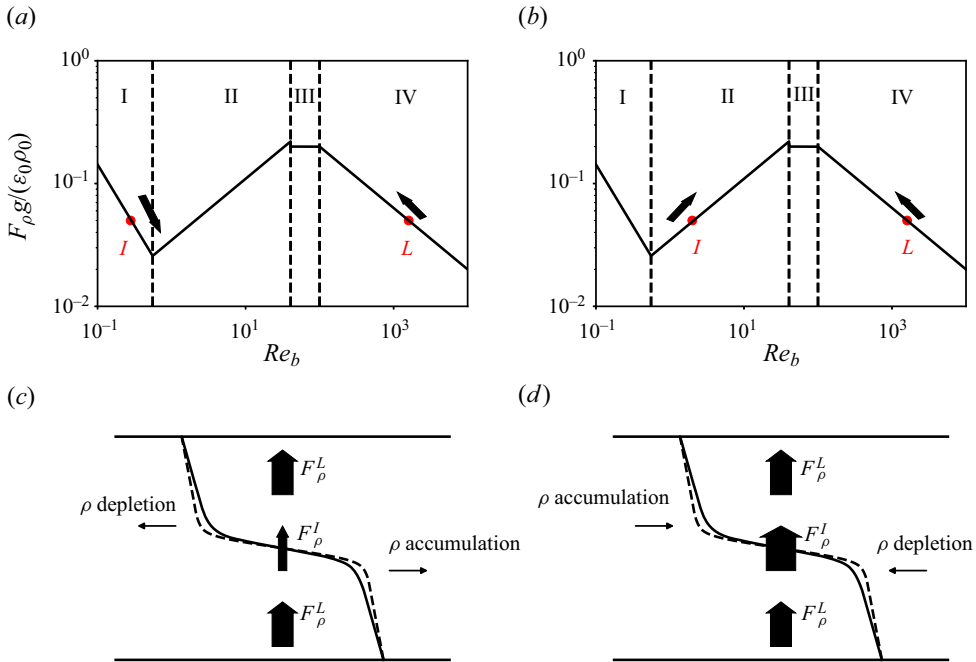


Figure 12. (a,b) Dependence of buoyancy flux  $F_b$  on the buoyancy Reynolds number  $Re_b$  in the salinity-stratified fluid, based on the parameterisation by Bouffard & Boegman (2013) with  $Sc = 70$ . The red dots labelled ‘I’ and ‘L’ represent the possible positions of interfaces and layers in the parameter space, respectively. Panel (a) illustrates an example of a stable configuration, while panel (b) depicts an example of an unstable configuration. (c,d) Schematic representations of the stable staircase structure vs the unstable staircase structure. The dashed black curve displays the original density profile, and the solid black curve represents the perturbed density profile. The effect of density perturbations on  $F_b$  is indicated by the change in vertical arrows from black to orange.

above the interface, thus generating a negative feedback to the perturbation. Similarly, an analogous argument applies to the inverse type of perturbation, where  $|\rho_z^L|$  decreases and  $|\rho_z^I|$  increases. In this case, the resulting flux laws will cause an increase of  $F_{\rho}^I$  and decrease  $F_{\rho}^L$ , thereby also creating a negative feedback mechanism. Consequently, under both types of perturbations, the staircase structure depicted in figure 12(a) remains stable. Conversely, in the situation presented in figure 12(b), the decrease of  $|\rho_z^I|$  leads to an increase in  $F_{\rho}^I$ . Under this condition, it is possible to have a specific perturbation  $(\rho_z^I, \rho_z^L)$  such that  $F_{\rho}^I$  becomes even larger than  $F_{\rho}^L$ , as shown in figure 12(d). These fluxes induce positive feedback to the perturbation, causing the continuous decrease of the interface gradients, which eventually disrupts the staircase structure.

Therefore, in order to maintain a stable staircase structure, the interface must be strongly stratified, ensuring it remains in region I. Physically, the staircase structure will remain stable if the turbulence strength is weak, allowing the interfacial transport to be dominated by molecular diffusion. However, the staircase structure will become unstable if the turbulence is strong enough to penetrate the interface and initiate a positive feedback loop. This explains why the staircase is disrupted at a strong turbulence level.

Several aspects should be emphasised regarding the stability model for turbulence-maintained staircases presented previously. First, it is important to note that the model does not necessitate Bouffard & Boegman’s (2013) parameterisation to be precisely accurate.

Provided that the four mixing regimes exist and exhibit the correct trends of increasing or decreasing fluxes with respect to changes in stratification, the argument remains valid and offers a reasonable explanation for the stability of turbulence-maintained staircases. Second, it should be highlighted that the simple stability analysis above cannot yet be utilised to establish a quantitative criterion distinguishing between staircase disruption and maintenance regimes. This is due to the uncertainty surrounding the current value of  $Re_b = 0.56$ , which separates regimes I and II in (3.3) (see the discussion in Ma & Peltier 2022a), and the lack of a precise understanding of the factors determining the interface thickness in this context (it may be related to the Ozmidov scale, but sufficient data to support this claim are not available). Third, it is worth commenting on the relationship between the layer formation criterion derived in MP22 and a potential criterion for layer stability. Strictly speaking, the questions of whether the layering mode would spontaneously form from linear  $\Theta$  and  $S$  gradients and whether the staircase structure can stably exist are independent. However, if no stable configurations are present between a linear-gradient state and the staircase state in the system, it is plausible that whenever the linear-scalar-gradient configuration is unstable to the thermohaline turbulence instability described by MP22, it would always lead to the stable staircase structure. This possibility is partially supported by the observation that stable turbulence-maintained staircases are found in the parameter space of  $P \sim O(10)$  and  $P \sim O(1)$ , which is consistent with the thermohaline-turbulence instability criterion of  $0.6 < Re_b < 40$ , given that  $P \sim Re_b$  when the system is dominated by turbulence (see (2.3)).

It is worth mentioning that our model of turbulence-maintained staircases in the diffusive-convection regime, as described in this subsection, is not solely relevant to oceanographic staircases; it also provides a comprehensive description of the density staircases observed in laboratory experiments (e.g. Linden 1979; Ruddick, McDougall & Turner 1989). The single-component system characterising the density staircase problem represents a limiting case of our turbulence-maintained diffusive-convection staircases, where  $R_\rho$  approaches infinity and the fluid's density is determined entirely by its salinity. Our simulations with  $R_\rho = \infty$  can be regarded as representations of these lab experiments, given that initial laboratory experiments (e.g. Linden 1979) were conducted with salt concentration as well. Consequently, the thermohaline-turbulence theory presented in MP21 and MP22 also accurately describes the layer formation process of density staircases, which has been a critical topic in the study of stratified turbulence (see, e.g. Peltier & Caulfield 2003; Taylor & Zhou 2017; Caulfield 2021). In this subsection, we have further elaborated on the structure and stability of these density staircases. However, the primary focus of this paper remains on the thermohaline staircases in the Arctic Ocean, and we provide more details on what our numerical simulations imply for the diffusive-convection staircases found in the Arctic thermocline in the next section.

#### 4. Implications for Arctic staircases

In §§ 2 and 3, we have systematically presented our simulation results and analysed the staircase structures obtained from these simulations. In this section, we connect these discussions to the actual staircase structures observed in the Arctic Ocean.

##### 4.1. An estimation of timescales for the formation and disruption of Arctic staircases

In order to interpret the implications of our numerical simulations, it is necessary to perform a dimensional transformation to compare our numerical simulation results with the actual Arctic Ocean staircases.

Event	Non-dimensional time	Dimensional time
Staircase formation	2000–10 000	4–20 days
Staircase merging	1000–5000	2–10 days
Disruption by turbulence ( $P = 0.1$ )	100–300	5–13 hours
Disruption by double-diffusion	NA	$O(4 \text{ months})$

Table 2. Summary of non-dimensional and dimensional characteristic timescales of typical events of staircases in simulations.

As discussed in § 2, we have employed the characteristic length  $L_0$  and the buoyancy frequency  $N$  to non-dimensionalise our numerical system, with the Reynolds number  $Re = (U_0 L_0)/\nu = (L_0^2 N)/\nu$  fixed at 1000 in all of our simulations. Using the typical buoyancy frequency of  $N \sim 0.006 \text{ s}^{-1}$  in the Arctic pycnocline where staircases are present (e.g. Timmermans *et al.* 2008) and  $\nu = 1.8 \times 10^{-6} \text{ m}^2 \text{ s}^{-1}$ , we can immediately calculate  $L_0$  as

$$L_0 = \sqrt{Re \nu / N} = 0.55 \text{ m}. \quad (4.1)$$

Note that in MP22, we calculated  $L_0$  based on the typical dissipation rate  $\epsilon$  in the Arctic Ocean, arriving at a similar length scale value ( $L_0 \sim 0.33\text{m}$ ). Compared with that in MP22, the current dimensional transformation is more robust, considering that the spatial and temporal variations of  $N$  are much smaller than the variations of  $\epsilon$ .

By multiplying the non-dimensional step size and layer thicknesses by the above dimensional length scale, it can be estimated that the step sizes of the staircases are about 1–3 m, consistent with the step sizes of 1–5 m staircases measured in the Arctic Ocean (e.g. Timmermans *et al.* 2008). The thicknesses of the interfaces are approximately 0.05–0.15 m (temperature interfaces are slightly thinner than salinity interfaces), also in line with the measured interface thickness of 0.1 m (Padman & Dillon 1989). These consistencies, mentioned in MP22, are emphasised again here.

Using the timescale  $N \sim 0.006 \text{ s}^{-1}$  (e.g. Timmermans *et al.* 2008), we determined the timescales linked to the staircase formation, merging and disruption observed in our simulations. These details are presented in table 2. In addition, the table also shows the timescale for disruption caused by double-diffusion. Even though we did not simulate this process fully, we can estimate its timescale based on a typical length of 2 m and a temperature diffusivity of  $10^{-7} \text{ m}^2 \text{ s}^{-1}$ .

Although our simulations employed a compromise value of  $Sc = 70$ , the theory of thermohaline-turbulence instability described in MP22 suggests that these timescales would not significantly differ with a more typical value of  $Sc = 700$  (or higher) in our numerical models. Specifically, MP22 demonstrates, through simulations of the layer formation process in scenarios R2P10, R5P10, R8P10 and  $R\infty$ P10, that the rate of staircase formation and merging hinges on the growth rate derived from thermohaline instability theory. This rate, initially described in (2.6) of MP21, is shown to be independent of  $Sc$  as long as the  $Re_b$  values remain within the buoyancy-dominated regime defined by Bouffard & Boegman (2013) (the boundaries of this regime depends on  $Sc$ ). Furthermore, our analysis in § 3.3 indicates that the growth of disturbances potentially disrupting the staircases is influenced by the  $K_\rho$ – $Re_b$  scaling coefficient from the Bouffard & Boegman (2013) parameterisation, which is also independent of  $Sc$ . Thus, variations in  $Sc$  values would minimally affect these timescales according to our theoretical model.

However, this theoretical argument is established based on our simplified model, which requires confirmation through future simulations employing higher  $Sc$  values.

Interestingly, the timescale for staircase formation in our simulations is considerably shorter than what previous theories have estimated, which typically span several months to years (see, for example, Radko (2016) and Bebieva & Timmermans (2017)). While these earlier explanations lean towards timescales largely dictated by diffusivities nearing molecular diffusion rates, our theory and simulations suggest a much faster timescale determined by turbulent diffusivities as a consequence of involving active turbulence in our models. In our simulations, staircases can emerge within just a month, and their disruption can be even more rapid, taking place within a single day under strong turbulence. These fast response timescales imply that diffusive-convection staircases are acutely sensitive to surrounding turbulence levels. If this picture describes the Arctic environment, we should anticipate a robust correlation: strong turbulence likely correlates with the absence of staircases, whereas weaker turbulence is more conducive to their presence.

A clear indication of the staircases' response to changes in ambient turbulence levels is provided by the study of Guthrie *et al.* (2017). This work analysed four measurements taken in the Amundsen Basin of the Arctic Ocean between 2007 and April 2014. Notably, the authors observed extensive thermohaline staircases only in the 2013 survey. During this time, the turbulence levels, as gauged by microstructure measurements, were particularly low compared with other periods. This significant correlation between subdued turbulence and the existence of staircases aligns well with our previous discussion. However, it is worth noting that in the Arctic measurements, instances of staircase formation and disruption remain infrequent. An area worth further investigation is the distinct boundary separating regions with and without staircases, as highlighted in Boury *et al.* (2022). It is in these transitional areas where events leading to the formation or disruption of staircases might be more prevalent, although they were not observed in the initial survey of Boury *et al.* (2022).

#### 4.2. An updated criterion for stably persisting staircases in the Arctic Ocean

As demonstrated in MP21 and MP22, thermohaline-turbulence instability is responsible for transforming linear temperature and salinity stratification into a staircase configuration when the buoyancy Reynolds number ( $Re_b$ ) lies within the approximate range of 0.1 to 100. During the initial phase of staircase formation, stratified turbulence predominantly drives the system.  $F_b$  remains positive before staircases form, and double-diffusion is not a significant factor. Consequently, staircase formation depends exclusively on the background  $Re_b$  determined by the mean gradients of heat and salt, which could be regarded as an indicator of the external forcing  $P$  that drives the small-scale turbulence in real-world oceanographic settings.

However, as the system transitions into a staircase state, the sharp temperature and salinity gradients at the interfaces drive the formation of unstable boundary layers, and this is the point at which double-diffusion starts to play a role. The stability of the staircase state is subsequently also determined by the density ratio  $R_\rho$ . When  $R_\rho$  is below the critical value  $R_\rho^{cr} \approx 10$ , the staircases can endure provided the turbulence intensity remains moderate  $Re_b < 100$  and insufficient to disrupt them. Due to the substantial intermittency of Arctic turbulence, the value of  $Re_b$  may fluctuate, occasionally causing turbulent mixing to decrease substantially. Nevertheless, as demonstrated in our phase diagram (figure 2), low mixing levels will not result in staircase disruption as long as  $R_\rho$  is below the critical value  $R_\rho^{cr}$ .



Conversely, if  $R_\rho > R_\rho^{cr} \approx 10$ , staircases will be disrupted by diffusion when  $Re_b$  remains too low and formed again when  $Re_b$  stays at the range that satisfies thermohaline turbulence instability. Due to the strong intermittency of the Arctic turbulence (e.g. Dosser *et al.* 2021), the value of  $Re_b$  can vary over more than 3–4 order of magnitude and constantly to low values that are below  $O(1)$ . Therefore, the system experiences ongoing layer formation and disruption as the forcing strength varies considerably, and it is not a suitable regime for a persisting staircase structure to exist.

As a result, in order to find the persisting staircase structure in the Arctic Ocean, the following criterion that is based on both  $Re_b$  and  $R_\rho$  needs to be satisfied:

$$Re_b < 100, 1 < R_\rho < 10. \quad (4.2)$$

The turbulent strength measured by  $P$  needs to be smaller than approximately 100, and the background density ratio  $R_\rho$  has to be smaller than 10 as well.

In the Canada Basin where staircases are most abundant, the density ratio  $R_\rho$  has typical values of 2–9 (e.g. Shibley *et al.* 2017), which is smaller than  $R_\rho^{cr} \approx 10$ , suggesting that most of the observed staircases should be either considered as being in the double-diffusion-dominated regime or the hybrid regime in our phase diagram shown in figure 2, which is generally consistent with the criterion in (4.2). However, to achieve a more accurate comparison between our proposed criterion and the actual observations, more detailed analyses for  $Re_b$  and  $R_\rho$  need to be calculated in specific regions in the Arctic based on micro-structure measurements (e.g. Fine *et al.* 2022).

#### 4.3. Implications on the parameterisations of vertical heat transport

In this section, we discuss the implications of our numerical simulations for estimating heat transport in the Arctic staircases. The vertical heat flux across these staircases is a crucial factor in Arctic mixing, as the warm Atlantic water stored beneath the surface Arctic water has the potential to melt the entire Arctic sea ice if released to the surface (e.g. Rudels *et al.* 2004). The Arctic staircase structures, which are abundant in the Arctic thermocline, govern a significant portion of these heat fluxes.

Previous studies (e.g. Timmermans *et al.* 2008; Guthrie *et al.* 2015; Shibley *et al.* 2017) typically estimated heat flux across the Arctic staircases from the temperature and salinity profiles using the laboratory-based flux parameterisation of Kelley (1990) or the simulation-based flux parameterisation scheme of Flanagan *et al.* (2013). These parameterisation schemes have been found to underestimate the heat transport from the microstructure measurements. For example, Guthrie *et al.* (2015) showed that the observed fluxes across staircase structures were consistently higher than the parameterisations of both Kelley (1990) and Flanagan *et al.* (2013) by a factor of 2–4.

In light of our previous discussions, a potential source of discrepancy between parameterisation schemes and observations becomes evident. The foundational laboratory experiments by, e.g. Turner (1965) and Marmorino & Caldwell (1976), as elaborated upon in Kelley (1990), along with the numerical investigations in Flanagan *et al.* (2013), did not incorporate external forcing or background turbulence into the system. According to the classification proposed in the present study, such systems can be characterised as being solely driven by double-diffusion. As we illustrated in § 2.3, the vertical heat flux in regimes driven by both double-diffusion and turbulence can exhibit an enhancement of 2–6 times when juxtaposed against those driven by double-diffusion. Historically, the significant ramifications of turbulence on heat flux have been underrepresented in parameterisation approaches, a factor which can profoundly affect the assessment of the heat budget in Arctic surface waters.

The parameterisation schemes employed in ocean models, such as the KPP parameterisation, involve even more subtleties. In the KPP scheme, effective temperature diffusivities in the ocean interior below the mixed layer are introduced as follows:

$$K_{\theta}^{TOT} = K^{BG} + K^S + K^C + K^{SF} + K^{DC}, \quad (4.3)$$

where  $K^{BG}$  represents the background dissipation assumed to be induced by unresolved internal wave breaking,  $K^S$  corresponds to mixing driven by shear instability, which depends on the gradient Richardson number,  $K^C$  denotes mixing driven by convective instability, and  $K^{SF}$  and  $K^{DC}$  represent double-diffusive mixing due to salt-fingering and diffusive-convection, respectively. In the KPP scheme,  $K^{DC}$  is included to capture the heat transported by diffusive staircase structures. Its functional form is based on the laboratory experiment of Marmorino & Caldwell (1976) and the simple model of Fedorov (1988), taking the following form:

$$K^{DC} = 0.909\nu \exp(4.6 \exp(-0.54(R_{\rho} - 1))). \quad (4.4)$$

Although the KPP parameterisation was initially proposed in the 1990s, the decomposition method in (4.3) and the functional form of (4.4) are still employed to describe the contribution from diffusive-convection staircases, as seen in the POP ocean model by Smith *et al.* (2010) and the CVMix project by Griffies *et al.* (2015).

Irrespective of the specific functional formulas adopted, a potential concern may arise from the parameterisation of diffusivities in (4.3). This approach attempts to distinguish and treat mixing due to turbulence separately from the mixing influenced by the staircases. However, as underscored in our preceding discussion, the maintenance of staircases is intricately linked to the prevailing turbulence level in the system. Even within regimes where staircases are maintained, the mechanisms of heat transport vary significantly across different regions of the phase diagram (figure 2). Thus, it is imperative that the turbulence level be appropriately incorporated.

Based on our classification of different types of diffusive-convection staircases, we propose an alternative parameterisation method to be employed in ocean models to represent the underresolved vertical fluxes contributed from the staircases.

- (i) A criterion should be introduced to determine whether staircases may form at subgrid scales. This could be a form that depends on the turbulent levels and the background density ratio  $R_{\rho}$ , for example, shown in our (4.2).
- (ii) If the criterion predicts a non-staircase environment, the original mixing parameterisation form in (4.3) may continue to be used, but the  $K_{DC}$  component should be removed. Including this term in a region where staircases would not form could lead to an overestimation of vertical fluxes in global ocean models. For example, Peltier, Ma & Chandan (2020) found that  $K_{DC}$  significantly influences the fast warming transition in the Dansgaard–Oeschger relaxation oscillation by controlling the vertical heat flux that melts sea ice. The potential overestimation of  $K_{DC}$  in this example might explain the shorter period of Dansgaard–Oeschger oscillation cycles predicted in models.
- (iii) If the criterion predicts that staircases might form, a separate, unified functional form of  $K_{Stair}$  should be used instead to replace  $K^{BG} + K^S + K^{DC}$  in (4.3). The  $K_{Stair}$  will depend on both the estimated  $Re_b$  and background density ratio  $R_{\rho}$ .

This alternative approach to parameterising diffusivities for ocean models would necessitate continuously forced, staircase-resolved DNSs capable of supporting a low diffusivity ratio of at least  $\tau \sim 0.01$ . With our current model, achieving this is

computationally challenging due to the heightened resolution needed to accurately capture turbulence at the Batchelor's scale for salinity. Nonetheless, we are optimistic that this pathway holds promise for future investigations. As numerical methods advance or computational capacities expand, this could pave the way for a more accurate staircase parameterisation.

## 5. Summary and conclusions

In order to investigate the structure of the diffusive-convection staircases and the vertical heat transport across the staircases, we have performed a series of numerical simulations to explore the influence of density ratio  $R_\rho$  and the external forcing strength  $P$  on the staircase state that forms spontaneously in our numerical systems. By adjusting the value of  $P$  after a staircase is spontaneously formed from the thermohaline-turbulence instability described in Ma & Peltier (2022b) and Ma & Peltier (2022c), we found that the initial staircase state can either be maintained or disrupted when  $P$  is adjusted. Based on the energy sources of the system, we have further categorised all of our simulations into five regimes: the staircases can either be maintained in the double-diffusion-dominated regime, maintained in the turbulence-dominated regime, maintained in the hybrid regime, disrupted by diffusion or disrupted by turbulence.

We have then performed detailed analyses of the physical mechanism that maintained the staircase structure, in each of these regimes. In the double-diffusion driven regime, which corresponds to numerical simulations with no or weak external forcing, we have found that our numerical simulations are basically consistent with the theoretical model discussed initially by Linden & Shirtcliffe (1978). As described by Linden & Shirtcliffe (1978), the double-diffusion staircases are maintained by the critical structure of unstably stratified boundary layers above and below the interfaces. The buoyant or heavier elements contained in these boundary layers are then released into the unstably stratified mixed layers in the form of thin plumes. The boundary layers would only provide sufficient fluxes to balance the diffusion at the centre of the interface if the condition  $R_\rho < R_\rho^{cr}$  is satisfied, which is also confirmed in our numerical simulations. In the regime driven by both double-diffusion and turbulence, these boundary layers are still present. However, the introduction of turbulence mixes the plumes from boundary layers well into mixed layers, making the mixed layers unstably stratified. The fluxes transported by these staircases are also enhanced by the formation of an unstable density gradient in the mixed layers in this regime. Finally, in the turbulence-maintained regime, the boundary layer structure does not exist, and the staircase structure forms simply because the strongly stratified interface can reach the same flux level as the weakly stratified mixed layers. By performing a qualitative stability analysis under the idealised assumption of Bouffard & Boegman (2013), we have shown that the turbulence-maintained staircases may become unstable when the turbulence strength is high, in a way that is consistent with our numerical simulations.

The theoretical models presented in this paper provide a comprehensive perspective on the various interactions between turbulence and the diffusive-convection staircases. Turbulence does not just disrupt the diffusive-convection staircases; it also plays a pivotal role in sustaining them, whether in low or high  $R_\rho$  regimes. Its effect on staircase structures is evident in the nuances of the mixed-layer region. Depending on the primary mechanism supporting the staircases, the vertical density gradient within these layers can vary, becoming positive, negative or neutral, all influenced by the strength of turbulence introduced.

In this paper, along with our previous work Ma & Peltier (2022c), we have provided comprehensive explanations for the complete lifecycle of staircase structures in the ocean,

encompassing their formation, maintenance and eventual disruption. Our earlier studies established that layer formation is predominantly driven by thermohaline-turbulence instability, with a significant contribution from turbulence rather than double-diffusion. However, our current findings highlight the crucial role of double-diffusion in shaping the structure of these layers post-formation, particularly through the creation of boundary layer structures. Notably, these staircases are susceptible to disruption under strong ambient turbulence. In contrast to previous assumptions (e.g. Boury *et al.* 2022), we find that both the formation and disruption of these staircases occur at a much faster pace, primarily due to the influence of turbulence. By examining the conditions necessary for the formation and sustenance of layers, we propose a revised criterion for identifying persistent diffusive-convection staircases in the ocean. This criterion suggests that staircases are likely to persist when the buoyancy Reynolds number  $Re_b$  is less than 100 and the density ratio  $R_\rho$  is below 10.

Our work demonstrates a plausible approach for the calibration of the vertical fluxes contributed from staircase structure. We have shown that the staircase system driven by double-diffusion is fairly tolerant to the presence of finite-strength turbulence, which is consistent with the recent work by Brown & Radko (2022). This fact necessitates the accurate representation of the influence of turbulence on vertical heat flux across diffusive-convection staircases in parameterisations. Previous parameterisations based solely on double-diffusion-driven models may only provide a lower-bound estimation of vertical heat flux. A revised parameterisation that properly accounts for the role of turbulence on vertical heat flux through Arctic staircases is urgently needed to provide unbiased estimates.

The most straightforward future development of the current work, which we have mentioned several times in this paper, is to extend the diffusivity ratio  $\tau$  to the oceanographically relevant value of approximately 0.01 in order to accurately describe the real Arctic environment. By doing this, we will be able to obtain a more precise criterion for the conditions under which staircases can stably persist, as well as a more accurate parameterisation scheme for the vertical fluxes characteristic of these staircase structures. However, this would require much higher resolution in the numerical simulations, which we cannot afford to do at this time. Beyond the issue of the resolution, it is imperative to acknowledge that our simulations, as they stand, are somewhat tethered to the specific type of forcing employed. It could be valuable to assess the model's responses by experimenting with alternative forcing mechanisms. For instance, incorporating forcing in wave forms, as illustrated in Howland *et al.* (2020). The wave-form forcing channels energy into both the vertical kinetic and potential energy reservoirs, which could offer insightful juxtapositions for future studies.

**Acknowledgements.** We acknowledge the computing resources provided by Niagara cluster at the SciNet High Performance Computing facility at the University of Toronto funded by the Canadian Foundation for Innovation, the Province of Ontario and the University of Toronto. We thank three referees for their constructive comments.

**Funding.** Financial support under the NSERC Discovery grant A9627 is gratefully acknowledged.

**Declaration of interest.** The authors report no conflict of interest.

**Author ORCIDs.**

 Yuchen Ma <https://orcid.org/0000-0002-5829-6196>.

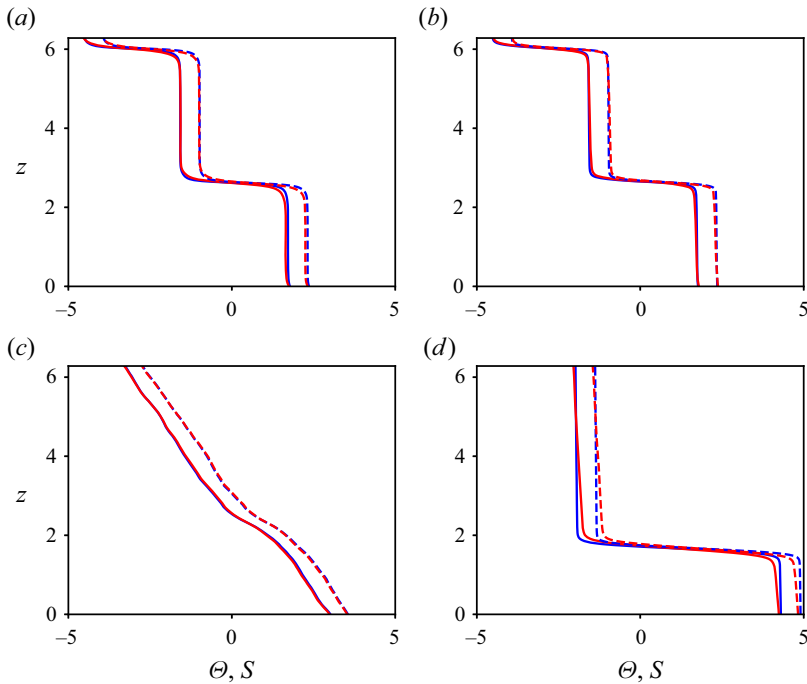


Figure 13. Comparison of horizontally averaged profiles for temperature (in red) and salinity (in blue) across different simulations. The intermediate-resolution simulations are represented by dashed lines, whereas the high-resolution simulations are depicted using solid lines. Profiles have been horizontally shifted to facilitate a clearer comparison. (a) R2P0, (b) R2P5, (c) R2P100 and (d) R8P5.

### Appendix. Influences of resolutions on vertical heat flux and salt flux in the simulations

In the main text, we conducted simulations at two distinct resolutions to investigate various aspects of the problem. An intermediate resolution of  $350 \times 350 \times 350$  was employed to capture the long-term evolution of the system, whereas a higher resolution of  $700 \times 700 \times 700$  was utilised to examine the staircase structure and fluxes. The high-resolution simulation has a grid size of approximately  $0.009L_0$  ( $L_0$  represents the non-dimensionalised length scale of our system). Although this grid size is smaller than the Kolmogorov scale, which varies from  $0.01L_0$  to  $0.03L_0$  depending on the value of  $p$ , it remains 2–8 times larger than the Batchelor scale for salinity of the system. Owing to computational power constraints preventing us from resolving the smallest scale of the system, it is crucial to examine the influence of resolution on our simulations by comparing the results between our intermediate- and high-resolution simulations.

The increase in resolution did not alter the staircase state of the system; specifically, upon increasing the resolution, no noticeable differences were observed in the horizontally averaged vertical profiles of temperature and salinity, as shown in figure 13. Nevertheless, the fluxes characterised by the Nusselt numbers  $Nu_\theta$ ,  $Nu_s$  and the flux ratio  $\gamma$  may be affected as the resolution changes. This is shown in figure 14(a,b), which displays the evolution of these quantities in the intermediate-resolution simulation and high-resolution simulation for R2P10, which is a configuration maintained in the hybrid regime. When the resolution was increased, the system re-equilibrated within a relatively short time frame ( $O(100)$  time units). In this new equilibrium state,  $Nu_\theta$ ,  $Nu_s$  and  $\gamma$  stabilise at a new level,

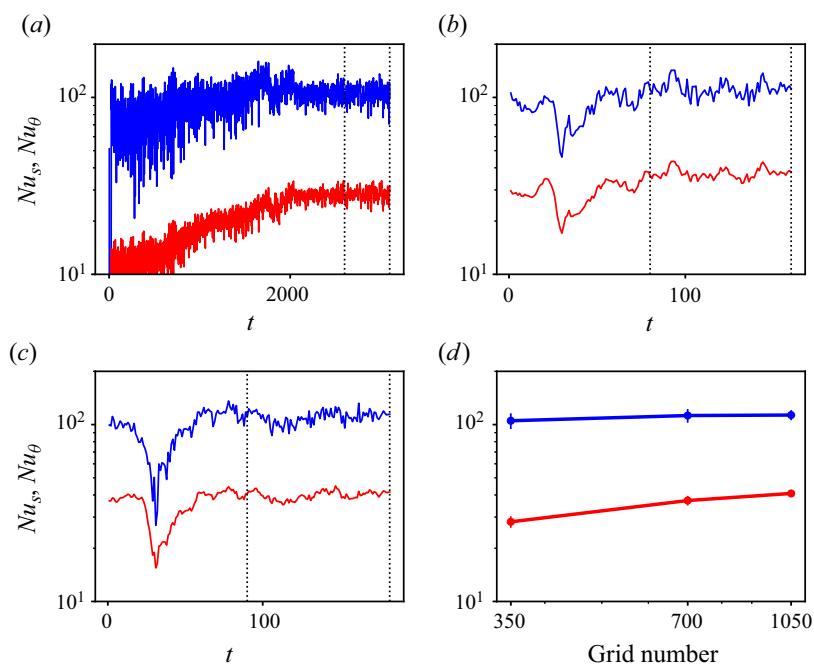


Figure 14. Evolution of  $Nu_\theta$  (red),  $Nu_s$  (blue) and  $\gamma$  in the intermediate-resolution simulation (a), high-resolution simulation (b) and a higher-resolution simulation (c) of R2P10, respectively. The two vertical dashed line in each figure marks the range of the equilibrium state that we use to calculate the average and standard deviation for each quantity. We presented a comparison of fluxes across different resolutions in panel (d), where the error bars depict the standard deviations.

which slightly differ from the original equilibrium values. To ensure flux convergence, we conducted a ‘higher-resolution simulation’ using a grid of  $1050 \times 1050 \times 1050$  in each dimension. This was achieved by extending the simulation from the equilibrium state of the high-resolution model. Owing to its intensive computational demands, we were only able to test this for the R2P10 simulation, as depicted in figure 14(c). Both the heat and salt fluxes stabilised to values nearly identical to those from our high-resolution simulation. This alignment confirms that our high-resolution simulations are closely representative of the converged value.

In table 3, we present the average values for  $Nu_\theta$ ,  $Nu_s$  and  $\gamma$  at the equilibrium state for both intermediate- and high-resolution simulations. We specifically highlight the quantities that are significantly influenced by the choice of resolution, which we define as an increase or decrease of more than 15 % when the resolution increases. In general, the fluxes are considerably influenced by resolutions in the double-diffusion-driven regime (e.g. R2P1, R2P5, R2P10, R3P0, R3P10 and R4P10). This might be due to the fact that the thin boundary layer structure above and below the interfaces, which occurs in the double-diffusion-driven regime, can only be accurately captured with sufficiently high resolutions. This is illustrated in figure 15, where the grid overlays the plumes close to the thin boundary layer, as detailed in the enlarged-view panel of figure 15(b). While the double-diffusive plumes are well-captured, the thin boundary layer, characterised by sharp density gradients, is represented with a more limited grid resolution. Conversely, in the turbulence-driven regime, particularly in simulations with high turbulence (e.g. R2P100, R5P50 and R5P100), an increase in resolution does not significantly affect the



Simulations	Resolution	Average period	$Nu_\theta$	$Nu_s$	$\gamma$
R2P0	Intermediate	500–4272	14.4 ± 1.1	37.9 ± 4.4	0.52 ± 0.03
	High	120–318	15.4 ± 0.9	34.5 ± 3.3	0.45 ± 0.02
R2P1	Intermediate	750–1504	17.4 ± 1.5	46.4 ± 5.2	<b>0.53 ± 0.02</b>
	High	80–249	19.6 ± 1.4	43.1 ± 4.2	<b>0.44 ± 0.02</b>
R2P5	Intermediate	200–1020	<b>22.2 ± 1.9</b>	69.9 ± 6.9	<b>0.63 ± 0.02</b>
	High	150–248	<b>28.0 ± 2.7</b>	69.8 ± 8.1	<b>0.50 ± 0.02</b>
R2P10	Intermediate	2600–3098	<b>28.2 ± 2.1</b>	105.1 ± 10.7	<b>0.74 ± 0.03</b>
	High	80–160	<b>37.2 ± 2.4</b>	112.4 ± 11.4	<b>0.60 ± 0.03</b>
	Higher	140–182	39.8 ± 2.2	110.1 ± 9.0	0.55 ± 0.02
R2P50	Intermediate	1200–1478	88.5 ± 7.0	424.7 ± 39.4	0.96 ± 0.03
	High	120–190	101.7 ± 7.6	443.8 ± 36.2	0.87 ± 0.02
R2P100	Intermediate	250–510	148.1 ± 10.8	1309.6 ± 109.0	1.77 ± 0.02
	High	40–110	150.8 ± 12.2	1363.6 ± 122.7	1.81 ± 0.02
R3P0	Intermediate	500–1998	15.4 ± 2.8	<b>25.5 ± 6.0</b>	0.49 ± 0.04
	High	120–377	14.3 ± 3.0	<b>20.2 ± 6.3</b>	0.42 ± 0.04
R3P10	Intermediate	11 500–12 526	<b>32.7 ± 3.7</b>	91.7 ± 10.9	<b>0.84 ± 0.02</b>
	High	120–207	<b>42.8 ± 3.4</b>	96.4 ± 8.7	<b>0.68 ± 0.02</b>
R4P10	Intermediate	10 000–10 918	28.5 ± 2.3	76.4 ± 7.2	<b>1.07 ± 0.04</b>
	High	270–319	31.7 ± 2.5	65.5 ± 6.1	<b>0.83 ± 0.03</b>
R5P5	Intermediate	600–2068	19.0 ± 1.5	36.0 ± 3.4	0.95 ± 0.03
	High	170–275	19.2 ± 1.8	31.3 ± 3.3	0.81 ± 0.03
R5P10	Intermediate	6000–8112	26.8 ± 2.3	69.5 ± 6.9	<b>1.29 ± 0.05</b>
	High	270–407	30.7 ± 2.7	63.5 ± 6.4	<b>1.04 ± 0.04</b>
R5P50	Intermediate	300–898	75.2 ± 4.8	396.6 ± 32.7	2.64 ± 0.10
	High	120–163	81.8 ± 5.8	409.6 ± 39.2	2.50 ± 0.08
R5P100	Intermediate	550–666	141.0 ± 9.6	1139.7 ± 87.7	4.04 ± 0.06
	High	90–146	141.8 ± 10.9	1200.1 ± 104.0	4.23 ± 0.06
R8P5	Intermediate	500–1944	16.4 ± 1.4	30.2 ± 3.2	1.47 ± 0.06
	High	250–391	16.9 ± 1.4	26.9 ± 2.6	1.27 ± 0.05
R8P10	Intermediate	5300–6298	25.1 ± 2.1	<b>64.0 ± 6.3</b>	<b>2.04 ± 0.08</b>
	High	350–400	27.4 ± 1.5	<b>53.8 ± 4.8</b>	<b>1.57 ± 0.08</b>
R∞P5	Intermediate	750–1674	NA	24.8 ± 2.8	NA
	High	140–294	NA	22.2 ± 2.6	NA
R∞P10	Intermediate	10 000–10 090	NA	56.4 ± 6.1	NA
	High	200–394	NA	50.7 ± 6.2	NA
R∞P50	Intermediate	300–540	NA	404.9 ± 38.3	NA
	High	45–151	NA	402.4 ± 34.3	NA
R∞P100	Intermediate	300–426	NA	1177 ± 100	NA
	High	40–91	NA	1296 ± 149	NA

Table 3. Averaged value for Nusselt numbers  $Nu_\theta$  and  $Nu_s$  and flux ratio  $\gamma$  at the equilibrium stage for our simulations. The error bars are calculated as standard deviations of each physical quantities in the equilibrium state. The values that increase/decrease over 15 % during an increase of resolution is highlighted using bold fonts.

fluxes, suggesting that the fluxes obtained from our simulations are more reliable for these scenarios.

Several other trends in [table 3](#) are worth noting. We observe that an increase in resolution consistently leads to an increase in  $Nu_\theta$ . In contrast,  $Nu_s$  decreases with resolution when  $P$  is small but increases with resolution when  $P$  is as large as 50 or 100. The underlying mechanism for how the change in numerical resolution leads to this systematic alteration of vertical fluxes remains unclear to us. However, this observation provides a means to

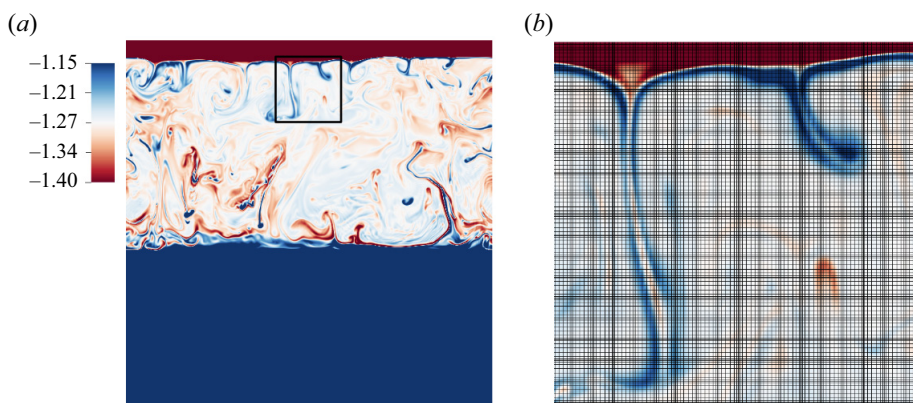


Figure 15. (a) Pseudo-colour plot of density field for the equilibrium staircases in the high-resolution simulation of R2P0. This plot shows the two-dimensional slice of the same field of figure 4 in the main text. (b) Enlarged view of panel (a) with mesh information plotted on top.

narrow down the possible true values for fluxes when inaccuracies arise from insufficient resolution.

Finally, we want to emphasise that the potential inaccuracies in the Nusselt numbers discussed here do not undermine the discussions in the main text of our paper. Our primary objective was not to provide a simulation-based parameterisation for fluxes across the Arctic staircase that can be directly employed in the observations. Instead, the goal of this paper is to establish a robust theoretical framework to describe the complex interactions between turbulence and diffusive-convection staircase, as well as to lay the foundation for the possibility of obtaining properly designed simulation-based parameterisation schemes in the future.

#### REFERENCES

- AHLERS, G., GROSSMANN, S. & LOHSE, D. 2009 Heat transfer and large scale dynamics in turbulent Rayleigh–Bénard convection. *Rev. Mod. Phys.* **81** (2), 503.
- BEBIEVA, Y. & TIMMERMANS, M.-L. 2017 The relationship between double-diffusive intrusions and staircases in the Arctic Ocean. *J. Phys. Oceanogr.* **47** (4), 867–878.
- BOUFFARD, D. & BOEGMAN, L. 2013 A diapycnal diffusivity model for stratified environmental flows. *Dyn. Atmos. Oceans* **61**, 14–34.
- BOURY, S., SUPEKAR, R., FINE, E.C., MUSGRAVE, R., MICKETT, J.B., VOET, G., ODIER, P., PEACOCK, T., MACKINNON, J.A. & ALFORD, M.H. 2022 Observations of double diffusive staircase edges in the Arctic Ocean. *J. Geophys. Res.: Oceans* **127** (11), e2022JC018906.
- BROWN, J.M. & RADKO, T. 2019 Initiation of diffusive layering by time-dependent shear. *J. Fluid Mech.* **858**, 588–608.
- BROWN, J.M. & RADKO, T. 2021 Diffusive staircases in shear: dynamics and heat transport. *J. Phys. Oceanogr.* **51** (6), 1915–1928.
- BROWN, J.M. & RADKO, T. 2022 Disruption of Arctic staircases by shear. *Geophys. Res. Lett.* **49** (20), e2022GL100605.
- CARPENTER, J.R., SOMMER, T. & WÜEST, A. 2012 Simulations of a double-diffusive interface in the diffusive convection regime. *J. Fluid Mech.* **711**, 411–436.
- CAULFIELD, C.-P. 2021 Layering, instabilities, and mixing in turbulent stratified flows. *Annu. Rev. Fluid Mech.* **53**, 113–145.
- COLE, S.T., TOOLE, J.M., RAINVILLE, L. & LEE, C.M. 2018 Internal waves in the arctic: influence of ice concentration, ice roughness, and surface layer stratification. *J. Geophys. Res.: Oceans* **123** (8), 5571–5586.
- CRAPPER, P.F. 1975 Measurements across a diffusive interface. In *Deep Sea Research and Oceanographic Abstracts*, vol. 22, pp. 537–545. Elsevier.

- DOSSER, H.V., CHANONA, M., WATERMAN, S., SHIBLEY, N.C. & TIMMERMANS, M.-L. 2021 Changes in internal wave-driven mixing across the Arctic Ocean: finescale estimates from an 18-year pan-Arctic record. *Geophys. Res. Lett.* **48** (8), e2020GL091747.
- FEDOROV, K.N. 1988 Layer thicknesses and effective diffusivities in ‘diffusive’ thermohaline convection in the ocean. In *Elsevier Oceanography Series*, vol. 46, pp. 471–479. Elsevier.
- FINE, E.C., MACKINNON, J.A., ALFORD, M.H. & MICKETT, J.B. 2018 Microstructure observations of turbulent heat fluxes in a warm-core Canada Basin eddy. *J. Phys. Oceanogr.* **48** (10), 2397–2418.
- FINE, E.C., MACKINNON, J.A., ALFORD, M.H., MIDDLETON, L., TAYLOR, J., MICKETT, J.B., COLE, S.T., COUTO, N., BOYER, A.L. & PEACOCK, T. 2022 Double diffusion, shear instabilities, and heat impacts of a Pacific summer water intrusion in the Beaufort Sea. *J. Phys. Oceanogr.* **52** (2), 189–203.
- FISCHER, P.F., KRUSE, J., LOTTES, J.W. & KERKEMEIER, S.G. 2008 Nek5000. <http://nek5000.mcs.anl.gov>.
- FLANAGAN, J.D., LEFLER, A.S. & RADKO, T. 2013 Heat transport through diffusive interfaces. *Geophys. Res. Lett.* **40** (10), 2466–2470.
- FLANAGAN, J.D., RADKO, T., SHAW, W.J. & STANTON, T.P. 2014 Dynamic and double-diffusive instabilities in a weak pycnocline. Part II: direct numerical simulations and flux laws. *J. Phys. Oceanogr.* **44** (8), 1992–2012.
- GRIFFIES, S.M., LEVY, M., ADCROFT, A.J., DANABASOGLU, G., HALLBERG, R.W., JACOBSEN, D., LARGE, W. & RINGLER, T. 2015 Theory and numerics of the Community Ocean Vertical Mixing (CVMix) project. *Tech. Rep.* <https://github.com/CVMix/CVMix-description>.
- GUO, S.-X., CEN, X.-R. & ZHOU, S.-Q. 2018 New parametrization for heat transport through diffusive convection interface. *J. Geophys. Res.: Oceans* **123** (2), 1327–1338.
- GUTHRIE, J.D., FER, I. & MORISON, J. 2015 Observational validation of the diffusive convection flux laws in the Amundsen Basin, Arctic Ocean. *J. Geophys. Res.: Oceans* **120** (12), 7880–7896.
- GUTHRIE, J.D., FER, I. & MORISON, J.H. 2017 Thermohaline staircases in the Amundsen Basin: possible disruption by shear and mixing. *J. Geophys. Res.: Oceans* **122** (10), 7767–7782.
- HOWLAND, C.J., TAYLOR, J.R. & CAULFIELD, C.P. 2020 Mixing in forced stratified turbulence and its dependence on large-scale forcing. *J. Fluid Mech.* **898**, A7.
- KELLEY, D.E. 1990 Fluxes through diffusive staircases: A new formulation. *J. Geophys. Res.: Oceans* **95** (C3), 3365–3371.
- KELLEY, D.E., FERNANDO, H.J.S., GARGETT, A.E., TANNY, J. & ÖZSOY, E. 2003 The diffusive regime of double-diffusive convection. *Prog. Oceanogr.* **56** (3–4), 461–481.
- KRISHFIELD, R., TOOLE, J., PROSHUTINSKY, A. & TIMMERMANS, M.-L. 2008 Automated ice-tethered profilers for seawater observations under pack ice in all seasons. *J. Atmos. Ocean. Technol.* **25** (11), 2091–2105.
- LARGE, W.G., MCWILLIAMS, J.C. & DONEY, S.C. 1994 Oceanic vertical mixing: a review and a model with a nonlocal boundary layer parameterization. *Rev. Geophys.* **32** (4), 363–403.
- LINDEN, P.F. 1979 Mixing in stratified fluids. *Geophys. Astrophys. Fluid Dyn.* **13** (1), 3–23.
- LINDEN, P.F. & SHIRTCLIFFE, T.G.L. 1978 The diffusive interface in double-diffusive convection. *J. Fluid Mech.* **87** (3), 417–432.
- MA, Y. & PELTIER, W.R. 2022a Diapycnal diffusivities in Kelvin–Helmholtz engendered turbulent mixing: the diffusive–convection regime in the Arctic Ocean. *J. Fluid Mech.* **946**, A32.
- MA, Y. & PELTIER, W.R. 2022b Thermohaline staircase formation in the diffusive convection regime: a theory based upon stratified turbulence asymptotics. *J. Fluid Mech.* **931**, R4.
- MA, Y. & PELTIER, W.R. 2022c Thermohaline-turbulence instability and thermohaline staircase formation in the polar oceans. *Phys. Rev. Fluids* **7** (8), 083801.
- MAFFIOLI, A., BRETHER, G. & LINDBORG, E. 2016 Mixing efficiency in stratified turbulence. *J. Fluid Mech.* **794**, R3.
- MAKSYM, T. 2019 Arctic and Antarctic sea ice change: contrasts, commonalities, and causes. *Annu. Rev. Mar. Sci.* **11** (1), 187–213.
- MARMORINO, G.O. & CALDWELL, D.R. 1976 Heat and salt transport through a diffusive thermohaline interface. In *Deep Sea Research and Oceanographic Abstracts*, vol. 23, pp. 59–67. Elsevier.
- MERRYFIELD, W.J. 2000 Origin of thermohaline staircases. *J. Phys. Oceanogr.* **30** (5), 1046–1068.
- NEAL, V.T., NESHYBA, S. & DENNER, W. 1969 Thermal stratification in the Arctic Ocean. *Science* **166** (3903), 373–374.
- NEWELL, T.A. 1984 Characteristics of a double-diffusive interface at high density stability ratios. *J. Fluid Mech.* **149**, 385–401.
- PADMAN, L. & DILLON, T.M. 1987 Vertical heat fluxes through the Beaufort Sea thermohaline staircase. *J. Geophys. Res.: Oceans* **92** (C10), 10799–10806.

- PADMAN, L. & DILLON, T.M. 1989 Thermal microstructure and internal waves in the Canada Basin diffusive staircase. *Deep Sea Res. A. Oceanogr. Res. Papers* **36** (4), 531–542.
- PELTIER, W.R. & CAULFIELD, C.P. 2003 Mixing efficiency in stratified shear flows. *Annu. Rev. Fluid Mech.* **35** (1), 135–167.
- PELTIER, W.R., MA, Y. & CHANDAN, D. 2020 The KPP trigger of rapid AMOC intensification in the nonlinear Dansgaard–Oeschger relaxation oscillation. *J. Geophys. Res.: Oceans* **125** (5), e2019JC015557.
- RADKO, T. 2007 Mechanics of merging events for a series of layers in a stratified turbulent fluid. *J. Fluid Mech.* **577**, 251–273.
- RADKO, T. 2013 *Double-Diffusive Convection*. Cambridge University Press.
- RADKO, T. 2016 Thermohaline layering in dynamically and diffusively stable shear flows. *J. Fluid Mech.* **805**, 147–170.
- RADKO, T. 2019 Thermohaline-shear instability. *Geophys. Res. Lett.* **46** (2), 822–832.
- RUDDICK, B.R., MCDUGALL, T.J. & TURNER, J.S. 1989 The formation of layers in a uniformly stirred density gradient. *Deep Sea Res. A. Oceanogr. Res. Papers* **36** (4), 597–609.
- RUDELS, B., JONES, E.P., SCHAUER, U. & ERIKSSON, P. 2004 Atlantic sources of the Arctic Ocean surface and halocline waters. *Polar Res.* **23** (2), 181–208.
- SHIBLEY, N.C. & TIMMERMANS, M.-L. 2019 The formation of double-diffusive layers in a weakly turbulent environment. *J. Geophys. Res.: Oceans* **124** (3), 1445–1458.
- SHIBLEY, N.C., TIMMERMANS, M.-L., CARPENTER, J.R. & TOOLE, J.M. 2017 Spatial variability of the Arctic Ocean’s double-diffusive staircase. *J. Geophys. Res.: Oceans* **122** (2), 980–994.
- SHIH, L.H., KOSEFF, J.R., IVEY, G.N. & FERZIGER, J.H. 2005 Parameterization of turbulent fluxes and scales using homogeneous sheared stably stratified turbulence simulations. *J. Fluid Mech.* **525**, 193–214.
- SHIRTCLIFFE, T.G.L. 1973 Transport and profile measurements of the diffusive interface in double diffusive convection with similar diffusivities. *J. Fluid Mech.* **57** (1), 27–43.
- SMITH, R., *et al.* 2010 The Parallel Ocean Program (POP) reference manual: ocean component of the community climate system model (CCSM) and community earth system model (CESM). LAUR-01853, vol. 141, pp. 1–140.
- SOMMER, T., CARPENTER, J.R. & WÜEST, A. 2014 Double-diffusive interfaces in Lake Kivu reproduced by direct numerical simulations. *Geophys. Res. Lett.* **41** (14), 5114–5121.
- TAYLOR, J. 1988 The fluxes across a diffusive interface at low values of the density ratio. *Deep Sea Res. A. Oceanogr. Res. Papers* **35** (4), 555–567.
- TAYLOR, J.R. & ZHOU, Q. 2017 A multi-parameter criterion for layer formation in a stratified shear flow using sorted buoyancy coordinates. *J. Fluid Mech.* **823**, R5.
- TIMMERMANS, M.-L., TOOLE, J., KRISHFIELD, R. & WINSOR, P. 2008 Ice-tethered profiler observations of the double-diffusive staircase in the Canada Basin thermocline. *J. Geophys. Res.: Oceans* **113** (C1), C00A02.
- TOOLE, J.M., KRISHFIELD, R.A., TIMMERMANS, M.-L. & PROSHUTINSKY, A. 2011 The ice-tethered profiler: argo of the Arctic. *Oceanography* **24** (3), 126–135.
- TURNER, J.S. 1965 The coupled turbulent transports of salt and heat across a sharp density interface. *Intl J. Heat Mass Transfer* **8** (5), 759–767.
- VAN DER BOOG, C.G., DIJKSTRA, H.A., PIETRZAK, J.D. & KATSMAN, C.A. 2021 Double-diffusive mixing makes a small contribution to the global ocean circulation. *Commun. Earth Environ.* **2** (1), 1–9.
- WAITE, M.L. & BARTELLO, P. 2004 Stratified turbulence dominated by vortical motion. *J. Fluid Mech.* **517**, 281–308.
- YANG, Y., VERZICCO, R., LOHSE, D. & CAULFIELD, C.P. 2022 Layering and vertical transport in sheared double-diffusive convection in the diffusive regime. *J. Fluid Mech.* **933**, A30.